Materials Science & Engineering A 856 (2022) 143898

Contents lists available at ScienceDirect

Materials Science & Engineering A

journal homepage: www.elsevier.com/locate/msea

Elucidating dynamic precipitation and yield strength of rolled Mg–Al–Ca–Mn alloy

Jiehua Li [a,b,*], Xuyang Zhou [a], Jing Su [a], Benjamin Breitbach [a], Marta Lipińska Chwałek [c,d], Huiyuan Wang [e], Gerhard Dehm [a]

[a] Max-Planck Institut für Eisenforschung, Max-Planck-Strasse 1, D-40237, Düsseldorf, Germany
[b] Institute of Casting Research, Montanuniversität Leoben, A-8700, Leoben, Austria
[c] Central Facility for Electron Microscopy, RWTH Aachen University, 52074, Aachen, Germany
[d] Ernst Ruska-Centre (ER-C) for Microscopy and Spectroscopy with Electrons, Forschungszentrum Jülich GmbH, 52425, Jülich, Germany
[e] Key Laboratory of Automobile Materials of Ministry of Education, School of Materials Science and Engineering & International Center of Future Science, Jilin University, No. 5988 Renmin Street, Changchun, 130025, PR China

ARTICLE INFO

Keywords:
Mg alloy
Dynamic precipitation
Dynamical recrystallization
Yield strength
Texture
Transmission electron microscopy
Atom probe tomography

ABSTRACT

Although the precipitation and recrystallization of Mg–Al–Ca–Mn based alloys have been well investigated individually, there is still a lack of a detailed investigation on the effect of the Al-rich clusters, Mn-rich precipitates and/or Ca-rich Laves phases formed from dynamic precipitation during rolling on the grain size and texture as well as yield strength. Here, we have investigated the effect of Mn (1 wt. %) on the dynamic precipitation and yield strength of rolled Mg–3Al–1Ca alloy after rolling up to 1 and 6 passes (at 350 °C and 300 °C). It was found that an effective grain refinement can be obtained due to the fact that the dynamic precipitation enhances dynamic recrystallization by particle stimulated nucleation (PSN) mechanism. No significant texture change was obtained although the dynamic precipitation of Mn-rich particles due to the addition of 1 wt. % Mn results in a change from an RD-split texture to a strong basal texture. Three different Mn-rich phases ((i) large primary Al_8Mn_5 phase, (ii) the long plated-shaped Al_8Mn_5 phase, and (iii) nanoscale Al_8Mn_5 phase), C15 Laves phase (Al_2Ca) and Al-rich clusters (G.P. zone), were observed, while no plate-shaped Al–Ca precipitate was observed on the basal plane of α-Mg matrix, indicating a competition among the formation of Al-rich clusters, plate-like Al–Ca precipitates, Ca-rich Laves phase, and Mn–rich phase within α-Mg matrix. Dispersion strengthening by the Ca-rich Laves phase, Mn–rich phase and Al-rich clusters is proposed to be attributed to the significant improvement of yield strength. This investigation highlights the importance of elucidating the effect of the dynamic precipitation on yield strength of rolled Mg–3Al–1Ca–1Mn alloys and provides helpful hints to further optimize the deformation and mechanical properties of Mg–Al–Ca–Mn based alloys.

1. Introduction

Mg alloy, as the lightest structural metal material, has irreplaceable advantages and has been widely used in aerospace, automotive, consumer electronic, sporting and transport devices due to its strength to weight ratio, good strength at room temperature, relatively large thermal and electrical conductivities [1]. The addition of rare earth (RE) elements can dramatically improve the mechanical properties of Mg alloys, but these RE elements are expensive and therefore not suitable for practical vast application in the costs-sensitive automotive industry. To date, most commercial Mg alloys are still based on Mg–Al alloys (i.e. AZ91, AZ31, AM60), which are one of the most important Mg alloys due to their low costs and adequate mechanical properties at room temperature. However, the mechanical properties of conventional Mg–Al based alloys at elevated temperatures (i.e., up to 120 °C) are not adequate due to the presence of $Mg_{17}Al_{12}$ phase, which can provide effective strengthening effects of conventional Mg–Al based alloys only up to 120 °C [2]. How to reduce or avoid the formation of $Mg_{17}Al_{12}$ phase is a key point for the further development of Mg–Al based alloys.

Ca is a cost-effective alloying element and can increase strengths and ductility of Mg alloys by solid-solution strengthening, dispersion of precipitates, and decrease of anisotropy in critical resolved shear stress

* Corresponding author. Institute of Casting Research, Montanuniversität Leoben, A-8700, Leoben, Austria.
E-mail address: jiehua.li@unileoben.ac.at (J. Li).

https://doi.org/10.1016/j.msea.2022.143898
Received 20 June 2022; Received in revised form 25 August 2022; Accepted 26 August 2022
Available online 14 September 2022

[3–8]. Especially, Ca alloying of Mg–Al based alloys has been reported to have following advantages: (i) suppress the formation of $Mg_{17}Al_{12}$ phase via the formation of Ca-rich Laves phase (i.e. C36 $(Mg,Al)_2Ca$, C15 (Al_2Ca), C14 (Mg_2Ca)) and thereby greatly improve the strength of the alloy at elevated temperatures [9–24] (ii) improve the formability (i.e. extrusion and/or roll), via weakening the basal texture, which is similar to the effect of RE elements (i.e. Gd, Y) [3–8], (iii) increase the ignition temperature up to approximately 1040 °C due to the composite oxide layer consisting of CaO and MgO [25]. Benefitting from these advantages, Mg–Al–Ca based alloys have been widely investigated and used.

The addition of Mn into Mg–Al–Ca based alloy has also been reported to further improve the mechanical properties and the formability [25–36]. Dilute Mg–Al–Ca–Mn system could be extruded or rolled due to their excellent deformability [26,27]. It was found that the optimum Mn content in the Mg-0.3Ca-0.3Al alloy was 0.4 wt. %, which can achieve the high strength with a reasonable ductility due to the presence of high number density of G.P. zones within the fine grains [26]. The high strength is attributed to the combined effect of fine dynamically recrystallized grains pinned with fragmented Al–Ca or Mg–Ca intermetallic compounds, nanoscale plate-like Al–Ca precipitates, spherical Al–Mn–Ca precipitates and a strong basal texture [33,36]. Mg–Al–Ca–Mn alloys appear to be very promising to compete with Al alloy (6xxx) in the automotive application as next generation low-cost ultrahigh-strength wrought Mg alloys.

The further addition of Zn into Mg–Al–Ca–Mn alloy has also been reported to be beneficial for improving the mechanical properties and the formability [37–40]. It was found that the addition of a small amount of Zn (0.3 at. %) to the Mg–1.1Al–0.3Ca–0.2Mn alloy substantially improved the stretch formability [37]. A newly developed magnesium sheet alloy, Mg-1.1Al-0.3Ca-0.2Mn-0.3Zn (at. %), shows a large Index Erichsen value of 7.7 mm in a solution treated (T4) condition due to a weak basal texture [37]. Subsequent artificial ageing at 200 °C for 1 h (T6) significantly increases the 0.2% proof strength from 144 MPa to 204 MPa due to a dense distribution of monoatomic layer Guinier–-Preston zones on the basal planes of the Mg matrix [37].

However, at least three important issues remain still to be explored in Mg–Al–Ca–Mn alloy system: (i) there is a lack of a fundamental understanding of the formation of G.P. zones, nano-scale plate-like Al–Ca precipitates, spherical Al–Mn–Ca precipitates, Mn-rich precipitates and Ca-rich Laves phase upon multi-pass hot rolling of Mg–Al–Ca–Mn alloy (in particular at a higher Mn addition level (i.e. 1 wt. % Mn in the present investigation)). Also, the competition mechanisms in forming these phases within Mg matrix is unclear, (ii) the effect of multiple precipitates on the deformation microstructure (dynamic precipitation, dynamic recrystallization, texture evolution and grain size) still remains to be explored, especially the possible interaction between Mn-rich phase and Ca-rich Laves phase, and (iii) a detailed investigation on the effect of Mn addition on the yield strength after different rolling stages is still lacking.

The present investigation is aimed to elucidate these three important issues of Mg–Al–Ca–Mn alloy. A particular focus is on the effect of Mn on the dynamic precipitation and yield strength, elucidated with the aid of scanning electron microscopy (SEM) and electron backscattering diffraction (EBSD), X-ray diffraction analysis (XRD), high resolution scanning transmission electron microscopy (STEM) with high-angle annular dark-field (HAADF) imaging and energy-dispersive X-ray spectroscopy (EDS), atom probe tomography (APT) as well as digital image correlation (DIC). The present investigation can provide a fundamental understanding of the role of dynamic precipitation and its effect on yield strength, which is definitely helpful for the further development of high-performance Mg–Al–Ca–Mn alloys.

2. Experimental

Alloys with nominal compositions of Mg–3Al–1Ca and Mg–3Al–1Ca–1Mn (wt. %, used through the paper unless stated otherwise) were prepared from high purity Mg (99.9%), Al (99.9%), Mg–10Ca and Mg–10Mn master alloys. The alloys were melted in an electric resistance furnace under a protective-gas mixture (CO_2 with 1 vol% SF_6) and cast into a die mould (steel) at about 760 °C. Plates with a thickness of 6 mm were machined from the cast ingot and then homogenised. The homogenization treatment was performed at 500 °C for 20 h under a protection of Ar gas and followed by quenching into cold water. A subsequent rolling up to 6 passes was performed with a total thickness reduction of 76% and a final thickness of 1.4 mm. For the first, second, third, and fourth rolling passes, the samples were heated at 350 °C for 10 min before rolling. For the fifth and sixth rolling passes, the samples were heated at 300 °C for 10 min before rolling. The reason why a lower temperature (300 °C) was chosen for the fifth and sixth rolling passes is to obtain an effective grain refinement and thereby a smaller grain size (3–5 μm), which is of great necessity to further achieve the superplasticity (grain size <10 μm) [41]. The reduction level between each rolling pass is about 24%, 25%, 14%, 15%, 26%, 21% for Mg–3Al–1Ca alloy and 20%, 27%, 16%, 12%, 27%, 21% for Mg–3Al–1Ca–1Mn, respectively. Between each rolling pass, one sample was kept for subsequent microstructure characterisation (SEM and EBSD, TEM, APT), texture analysis (micro-texture via EBSD and macro-texture via XRD) and mechanical properties testing (DIC at room temperature). The same experimental procedure was applied to Mg–3Al–1Ca and Mg–3Al–1Ca–1Mn alloys. A comparative investigation on Mg–3Al–1Ca and Mg–3Al–1Ca–1Mn alloys is mainly aimed to elucidate the effect of Mn-alloying on the dynamic precipitation and yield strength of Mg–3Al–1Ca alloy.

Microstructures and micro-textures were characterized using Carl Zeiss Cross Beam 1540EsB equipped with HKL EBSD detector. The EBSD samples were metallographically prepared using SiC papers and 50 nm diameter silica suspension (water-free), and subsequently argon ion beam milled with a low voltage (2 kV) for 1 h using Hitachi IM4000 system. EBSD was performed with a step size of 0.05 μm (for rolled samples) and 0.2 μm (for as cast and homogenised samples). EBSD data analysis (including micro-texture analysis) was performed using TSL software (TSL Version 8.0).

In order to further investigate the macro-texture evolution, the Mg–3Al–1Ca and Mg–3Al–1Ca–1Mn alloys after different rolling passes (up to 6) were also characterized with XRD in a Seifert THETA-THETA diffractometer equipped with an ID3003 generator, a poly-capillary beam optic, a 4-circle goniometer, using Co-Kα radiation and an energy dispersive point detector. The Θ-2Θ overview measurements were carried out with a step size Δ2Θ of 0.05°, a count time of 1s/step. These overview measurements were used for qualitative phase analysis and determination of the reflex positions for the pole figure measurement. Pole figure measurements were done with a φ range of 0–360° about the rotation axis and a ψ range of 0–85° about the tilt axis with a step size of 5° each. Pole figures were measured at 2Θ values corresponding to Mg {100}, {002}, {101}, {110}, {103} and {122} poles. The texture data was analysed using the Matlab software package (MTEX Version 5.7.0) [42].

Tensile specimens with a gage length of 4 mm, gage width of 1.8 mm and thickness of 1 mm were machined from the as-rolled sheets along the rolling direction (RD). Tensile experiments of Mg–3Al–1Ca and Mg–3Al–1Ca–1Mn alloys after different rolling passes (up to 6) were conducted using a Kamrath & Weiss stage coupled with DIC technique with an initial strain rate of 1.0×10^{-3} s^{-1}. In each condition, at least two samples were tested. The average values were reported. Global and local strains were also measured by DIC.

TEM samples and APT specimens were prepared by a focused ion beam (FIB) lift-out method [43,44] in a FEI Helios Dual Beam SEM/FIB 600/600i instrument. Conventional TEM including selected area diffraction pattern (SADP) was performed using Tecnai G2 F20 operated at 200 kV. HAADF STEM imaging and EDS analyses were conducted with the aid of probe-corrected FEI Titan G2 80–200 operated at 200 kV. APT experiments were performed using a local electrode atom probe

(LEAP) 5096XR instrument (CAMECA Instruments, Madison, WI, USA) in a voltage-pulsed mode. The pulse repetition rate was 200 kHz and the target detection rate reached 5 detection events per 1000 pulses. The pressure in the analysis chamber at the level of 3×10^{-11} Torr and the specimen base temperature of 50 K were maintained during measurements. APT data reconstruction and analysis were performed using Imago Visualization and Analysis Software (AP Suite 6.1). The maximum separation method (MSM) was employed for the evaluation of the cluster characteristics [45–47]. In this method, a distance (d-max) is chosen. If pairs of solute atoms is less than this distance, they are considered as clusters. A threshold value for the minimum size of a cluster (N-min) was set to filter out the clusters from the random solid solution. A high-order nearest neighbour (NN) distribution (5NN) was also applied to increase the contrast between the matrix and clusters. In this work, a maximum distance between atoms (d-max) of 0.74–0.77 nm and a minimum number of solute atoms (N-min) of 12 were used.

3. Results

3.1. Microstructure in as cast condition

Fig. 1 shows SEM (backscatter (BS)) images of as-cast Mg–3Al–1Ca alloy (Fig. 1a) and Mg–3Al–1Ca–1Mn alloy (Fig. 1b), respectively. The Ca-rich Laves phase (C36 $(Mg,Al)_2Ca$, EBSD indexing is shown in Fig. S1) was observed to be continuously distributed along grain boundaries in both Mg–3Al–1Ca alloy and Mg–3Al–1Ca–1Mn alloy. However, in Mg–3Al–1Ca–1Mn alloy, Mn-rich phase (i.e. Al_8Mn_5) was also observed, as marked with a white arrow in Fig. 1b.

Fig. 2 shows inverse pole figure (IPF) maps and the corresponding measured grain size distribution of as-cast Mg–3Al–1Ca alloy (Fig. 2a and b) and Mg–3Al–1Ca–1Mn alloy (Fig. 2c and d), respectively. In both alloys, the grain size was measured to be about 43 ± 14 μm and 73 ± 39 μm, respectively. No significant grain refinement was observed with the addition of 1 wt. % Mn. Instead, a larger gain size was observed. The addition of 1 wt. % Mn is mainly related to the formation of Mn-rich phase (i.e. Al_8Mn_5) during solidification process, which cannot act as an effective nucleation site for α-Mg grain [48,49]. Instead, the formation of Mn-rich phase consumes the solute of Al thereby decrease the growth restriction factor (GRF, also known as Q) caused by Al [50] during solidification. The addition of 1 wt. % Ca can also be beneficial for the grain refinement of α-Mg grain due to its GRF (11.94 for Ca) [50]. At the early stage of solidification, the strong segregation ability of Ca results in the formation of constitutional undercooling in a diffusion layer ahead of the advancing solid/liquid interface which restricts grain growth and promotes nucleation in the melt. It should be noted that the grain size of 43 ± 14 μm and 73 ± 39 μm in both alloys is relatively smaller than that (more than 200 μm) in the conventional Mg–Al based alloys (i.e. AZ91, AZ31) in the same solidification condition (gravity die casting) [48], which can be mainly attributed to the effect of Ca (1 wt. %). The refined as-cast grain size is beneficial for the subsequent homogenization and rolling process.

3.2. Microstructure after homogenization

Fig. 3 shows IPF maps and the corresponding measured grain size distribution of homogenised Mg–3Al–1Ca alloy (Fig. 3a and b) and Mg–3Al–1Ca–1Mn alloy (Fig. 3c and d), respectively. In both alloys, the grain size was measured to be about 86 ± 32 μm and 93 ± 48 μm, respectively, indicating that a significant grain growth takes place during homogenization at 500 °C for 20 h, especially for Mg–3Al–1Ca alloy. It should be noted here that C15 Laves phase (C15 Al_2Ca, EBSD indexing is shown in Fig. S2) was observed in the homogenised Mg–3Al–1Ca alloy, strongly indicating that C36 Laves phase formed in as cast condition has transformed into C15 Laves phase during homogenization at 500 °C for 20 h.

3.3. Microstructure after rolling up to 6 passes

Fig. 4 shows IPF maps (Fig. 4a, d), kernel average misorientation (KAM) map (Fig. 4b, e) and the corresponding measured grain size distribution (Fig. 4c, f) of Mg–3Al–1Ca alloy (Fig. 4a–c) and Mg–3Al–1Ca–1Mn alloy (Fig. 4d–f) after the first rolling pass, respectively. The grain size was measured to be about 10.5 ± 8.9 μm and 7.2 ± 7.4 μm for Mg–3Al–1Ca alloy and Mg–3Al–1Ca–1Mn alloy, respectively. A smaller grain size was observed with the addition of 1 wt. % Mn. It should be noted here that the addition of 1 wt. % Mn increases the grain size in as-cast condition but decreases the grain size in rolled condition, which can be attributed to the enhanced dynamic recrystallization (DRX) by particle stimulated nucleation (PSN) mechanism during rolling. From the IPF maps (Fig. 4a, d) and KAM maps (Fig. 4b, e), few shear bands and twins (tensile twinning, see Fig. 5a, c, Figs. S3 and S4) were observed. Fine DRXed grains are distributed along these shear bands. The dislocations are more uniformly distributed and the density of dislocation in Mg–3Al–1Ca–1Mn alloy is also higher than those in Mg–3Al–1Ca alloy, as shown in KAM maps (Fig. 4b, e). In terms of the micro-texture, no significant deformation texture was observed after the first rolling pass, although the addition of Mn (1 wt. %) appears to increase the texture intensity from 18.983 m.r.d. (multiples of a random distribution) (max value for Mg–3Al–1Ca alloy) to 21.919 m.r.d. (max value for Mg–3Al–1Ca–1Mn alloy), as shown in Fig. 5b, d.

After the first rolling pass, the Ca-rich Laves phase of Mg–3Al–1Ca–1Mn alloy continuously distributed along grain boundaries has already been broken into small pieces. With increasing the rolling pass, the Ca-rich Laves phase becomes refiner and elongated

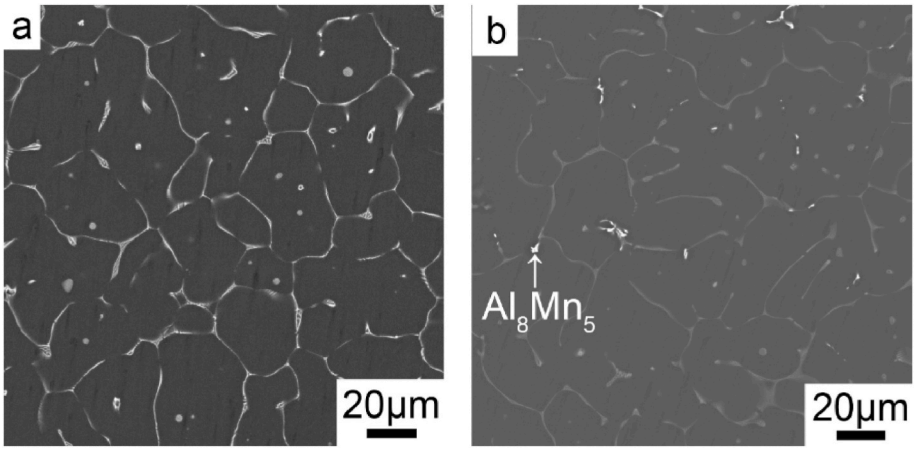

Fig. 1. Microstructure (SEM BS images) of as-cast samples. (a) Mg–3Al–1Ca alloy, (b) Mg–3Al–1Ca–1Mn alloy.

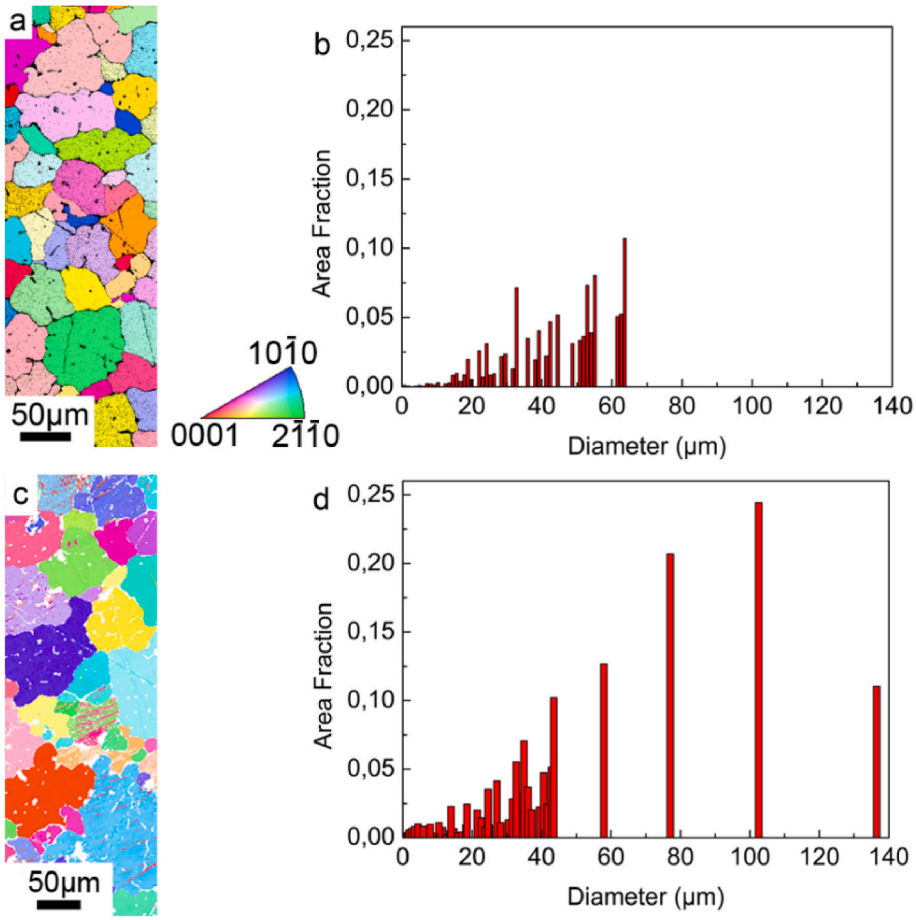

Fig. 2. IPF maps (a, c) and the corresponding measured grain size distribution (b, d) of as-cast samples. (a, b) Mg–3Al–1Ca alloy, (c, d) Mg–3Al–1Ca–1Mn alloy.

along the rolling direction (RD), which can be seen clearly from SEM images as shown in Fig. S5. Especially, after the fifth and sixth rolling pass at 300 °C, the Ca-rich Laves phase becomes much refiner compared with that after the fourth rolling pass, indicating the rolling temperature (350 °C for fourth rolling pass, 300 °C for the sixth rolling pass) has an important effect on the rolling microstructure. A quantitative analysis on the surface area fraction of second phases (Ca-rich Laves phases and Mn-rich phases) as a function of rolling pass (Fig. S6) shows that with increasing the rolling pass up to 4, a slight decrease of the surface area fraction of second phases was observed, while, after the fifth and sixth rolling pass, a significant increase of the surface area fraction of second phases was observed, which can be due to the lower rolling temperature (300 °C for the fifth and sixth rolling pass compared with 350 °C for the rolling pass up to 4). It should be noted here that a similar microstructure evolution was also observed in Mg–3Al–1Ca alloy. The following microstructure characterisation (EBSD, XRD, TEM and APT) mainly focus on the samples after the sixth rolling pass.

Fig. 6 shows IPF maps (Fig. 6a, d), KAM map (Fig. 6b, e) and the corresponding measured grain size distribution (Fig. 6c, f) of Mg–3Al–1Ca alloy after the sixth rolling pass (Fig. 6a–c) and Mg–3Al–1Ca–1Mn alloy after the sixth rolling pass (Fig. 6d–f), respectively. The grain size was measured to be about 6.0 ± 3.4 μm and 3.3 ± 2.1 μm for Mg–3Al–1Ca alloy and Mg–3Al–1Ca–1Mn alloy, respectively. Clearly, a significant grain refinement was observed with the addition of 1 wt. % Mn, which can be attributed to the enhanced dynamic recrystallization by PSN mechanism. It should be noted here that, in Mg–3Al–1Ca alloy, due to the absence of Al_8Mn_5 phase during rolling, the grain size Mg–3Al–1Ca alloy after the sixth rolling pass is larger than that of Mg–3Al–1Ca–1Mn alloy after the sixth rolling pass. In addition, from the KAM maps (Fig. 6b, e), it can be found that the Mg–3Al–1Ca–1Mn alloy recrystallizes more fully, which helps the grain refinement, as shown in Fig. 6c, f. In contrast to the presence of the tensile twinning after the first rolling pass, no significant deformation twins were identified, as shown in Figs. S7 and S8, which is due to twinning-induced dynamic recrystallization during rolling at 300 °C.

In terms of the micro-texture, Fig. 7 shows IPF maps (Fig. 7a, c) and the corresponding {0001}, {10 $\bar{1}$ 0}, {11$\bar{2}$ 0} pole figures (Fig. 7b, d) of Mg–3Al–1Ca alloy (Fig. 7a and b) and Mg–3Al–1Ca–1Mn alloy (Fig. 7c and d) after the sixth rolling pass, respectively. It should be noted here that the same EBSD measurement parameters in SEM (voltage (20 kV), step size (0.05 μm)) and the same size of analysis area was used in order to compare the texture intensity. The addition of Mn (1 wt. %) increases the texture intensity from 6.071 m.r.d. (max value for Mg–3Al–1Ca alloy) to 7.395 m.r.d. (max value for Mg–3Al–1Ca–1Mn alloy), indicating that the addition of Mn (1 wt. %) results in a strong texture. Furthermore, a careful observation on micro-texture shows that Mg–3Al–1Ca alloy has an RD-split texture (see two red poles along RD in Fig. 7b), while Mg–3Al–1Ca–1Mn has a strong basal texture. It should be noted that the {0002} pole figure is assumed to be sufficiently characteristic of the texture of the alloys as the distribution of other poles is distributed almost homogeneously circular around the c-axis. It should also be noted here that EBSD can be used to measure the micro-texture in a relative local region. It is still of great necessity to measure the macrotexture using XRD, which is more accurate as a much wider area can be scanned.

Fig. 8 shows {0002} pole figures of Mg–3Al–1Ca alloy and Mg–3Al–1Ca–1Mn alloy after the sixth rolling pass based on XRD measurements. Similar to Fig. 7, it was also found that Mg–3Al–1Ca alloy has an RD-split texture, which can be seen clearly in Fig. 8a (after the first rolling pass) and Fig. 8c (after the sixth rolling pass), while

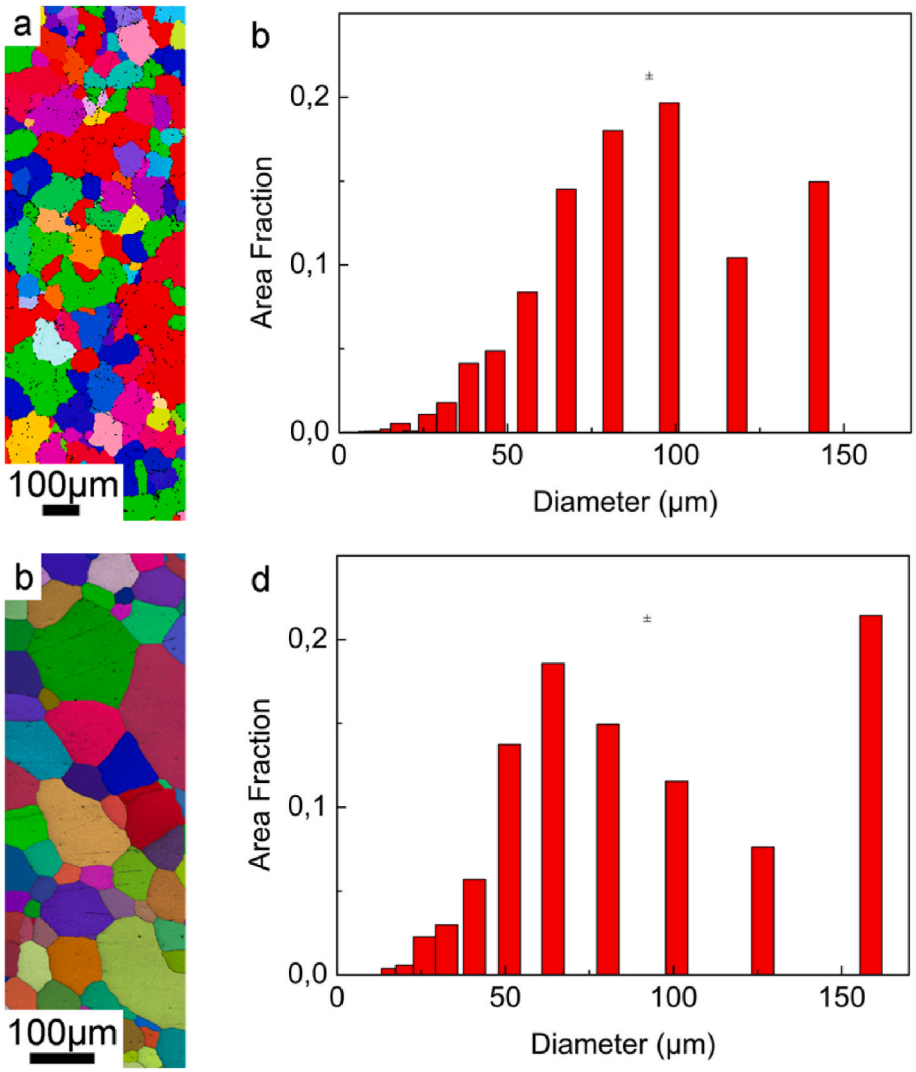

Fig. 3. IPF maps (a, c) and the corresponding measured grain size distribution (b, d) of homogenised samples (at 500 °C for 20 h). (a, b) Mg–3Al–1Ca alloy, (c, d) Mg–3Al–1Ca–1Mn alloy.

Mg–3Al–1Ca–1Mn has a strong basal texture, although an RD-split texture was also observed after the second rolling pass, as shown in Fig. S9. In both alloys, the texture intensity increases with increasing the rolling pass. For clarity, other recalculated prismatic pole figures taken from the corresponding {10 $\bar{1}$ 0}, {11$\bar{2}$ 0} are also shown in Figs. S10 and S11.

Apart from texture analysis, XRD was also used to index the phases and to determine the lattice parameters. Only Mg and Al_2Ca phases were measured by XRD, as shown in Fig. S12. Indexing Al_2Ca phases by XRD also indicates that the C36 ($(Mg,Al)_2Ca$) Laves phase has transformed into C15 (Al_2Ca) Laves phase after the sixth rolling pass, which is fully consistent with the EBSD indexing in Fig. S2. The absence of Al_8Mn_5 can be attributed to their trace amount, which can be not detected using XRD. Despite a strong texture in XRD, the volume fraction of Al_2Ca phase in both alloys was determined to be about 1.5%. However, it should be noted that, since Al_8Mn_5 forms as the primary phase during solidification, Al would be partly consumed and therefore less Al can react with Ca, which can be expected to decrease the volume fraction of Al_2Ca. Such a tiny decrease cannot be detected using XRD. Interestingly, the determination of the lattice parameter indicates that the presence of 1 wt. % Mn increases the lattice parameter (both a and c) slightly, as shown in Fig. S13. With increasing the rolling pass, the lattice parameter (both a and c) remains unchanged, indicating that the change of lattice parameter mainly depends on the alloy composition rather than the rolling temperature (350 °C for the first, second, third and fourth rolling pass, 300 °C for the fifth and sixth rolling pass) and rolling pass (up to 6).

3.4. Mechanical properties after rolling up to 6 passes

Fig. 9 shows mechanical properties of Mg–3Al–1Ca alloy and Mg–3Al–1Ca–1Mn alloy after the first rolling pass and sixth rolling pass. All results are measured using DIC. In terms of Mg–3Al–1Ca alloy, with increasing rolling pass from one to six, tensile strength (ultimate tensile strength) increases from 229 MPa to 247 MPa, the yield strength (0.2% proof stress) increases from 109 MPa to 218 MPa, while the elongation (elongation to failure) slightly increases from 11.6% to 13.0%. In terms of Mg–3Al–1Ca–1Mn alloy, with increasing rolling pass from one to six, tensile strength increases from 244 MPa to 246 MPa, the yield strength increases from 198 MPa to 220 MPa, while the elongation (elongation to failure) slightly increases from 12.2% to 13.3%. In both alloys, the elongation remains about 12–13%, which can be attributed to the fact that the addition of Ca decreases the barrier energy and the critical resolved shear stress ratios of higher-order deformation systems, increases the frequency of non-basal <c+a> slip more than that of <a> slip [3–8]. Compared with Mg–3Al–1Ca alloy after the first rolling pass, the tensile strength of Mg–3Al–1Ca–1Mn alloy after the first rolling pass

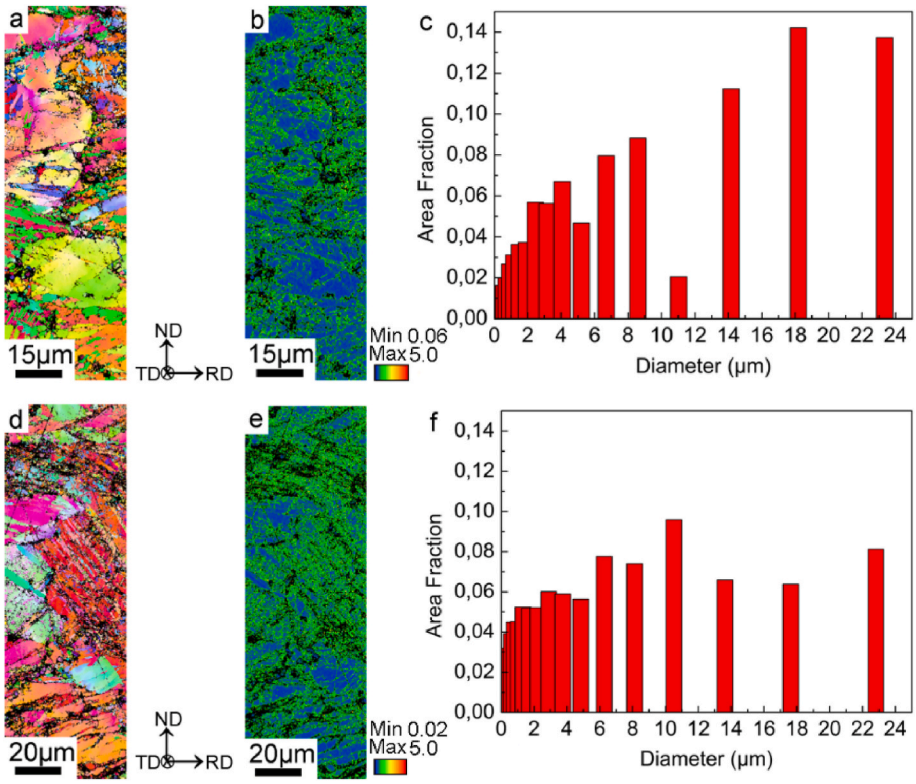

Fig. 4. IPF maps (a, d), KAM map (b, e), and the corresponding measured grain size distribution (c, f) of Mg–3Al–1Ca alloy (a–c) and Mg–3Al–1Ca–1Mn alloy (d–f) after the first rolling pass (with a total strain of 24% (Mg–3Al–1Ca alloy (a–c)) and 20% (Mg–3Al–1Ca–1Mn alloy (d–f)), at a temperature of 350 °C).

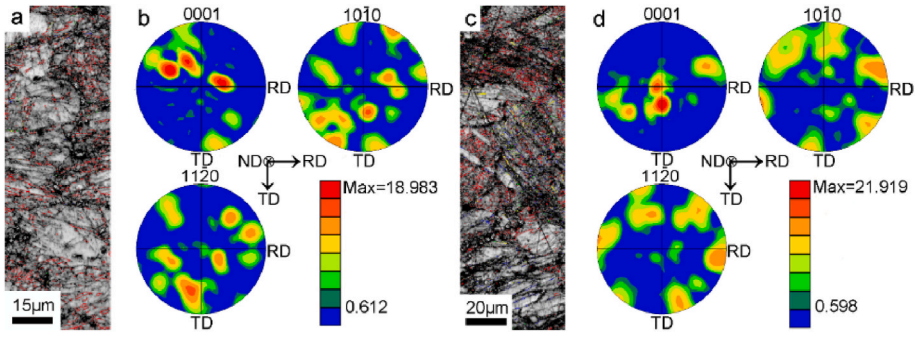

Fig. 5. Image quality (IQ) maps with the mark of twinning (a, c) and the corresponding {0001}, {10 $\bar{1}$ 0}, {11$\bar{2}$ 0} pole figures (b, d) of Mg–3Al–1Ca alloy (a, b) and Mg–3Al–1Ca–1Mn alloy (c, d) after the sixth rolling pass (with a total strain of 76% and at a temperature of 300 °C). The dataset in Fig. 5 is the same as Fig. 4. The same measurement parameters (voltage (20 kV), step size (0.05 μm)) and analysis area size was used in order to compare the texture intensity.

is higher (15 MPa), and the yield strength of Mg–3Al–1Ca–1Mn alloy after the first rolling pass is much higher (89 MPa), which can be related to the deformation microstructure characters as discussed in session 4. Compared with Mg–3Al–1Ca alloy after the sixth rolling pass, the tensile strength of Mg–3Al–1Ca–1Mn alloy after the sixth rolling pass is higher (28 MPa), and the yield strength of Mg–3Al–1Ca–1Mn alloy after the sixth rolling pass is only slightly higher (2 MPa). Furthermore, the addition of 1 wt. % Mn does not decrease the elongation (still at the level of 12–13%), which strongly indicates that the deformation microstructure of both two alloys after the sixth rolling pass would be similar. A detailed TEM and APT characterization on the Mg–3Al–1Ca–1Mn alloy after the sixth rolling pass is therefore needed to elucidate any possible difference caused by the presence of 1 wt. % Mn. Mg–3Al–1Ca alloy was not included here.

3.5. TEM characterisation on the Ca-rich Laves phase

Fig. 10 shows HAADF-STEM images and the corresponding fast Fourier transform (FFT) of C15 Laves phase (Al_2Ca) in Mg–3Al–1Ca–1Mn alloy after the sixth rolling pass. The determination of C15 Laves phase (Al_2Ca) can be further experimentally supported using the low magnification EDS maps (Fig. 10e–h) and the high magnification EDS maps (Fig. 10i-l). Viewed from $[011]_{Al2Ca}$ zone axis, an ordered structure was observed, as shown in Fig. 10c, i. The high magnification EDS maps (Fig. 10i-l) can clearly define the Al-rich and Ca-rich atomic columns. In addition, the large C15 Laves phase (Al_2Ca) was broken during rolling, as marked with a black arrow in Fig. 10a. In the vicinity of the large C15 Laves phase (Al_2Ca), various nanoscale Ca-rich precipitates (also C15 Laves phase (Al_2Ca)) formed during rolling via dynamic precipitation were also observed, as marked with a white arrow in Fig. 10a. Apart from the large C15 Laves phase (Al_2Ca), in the

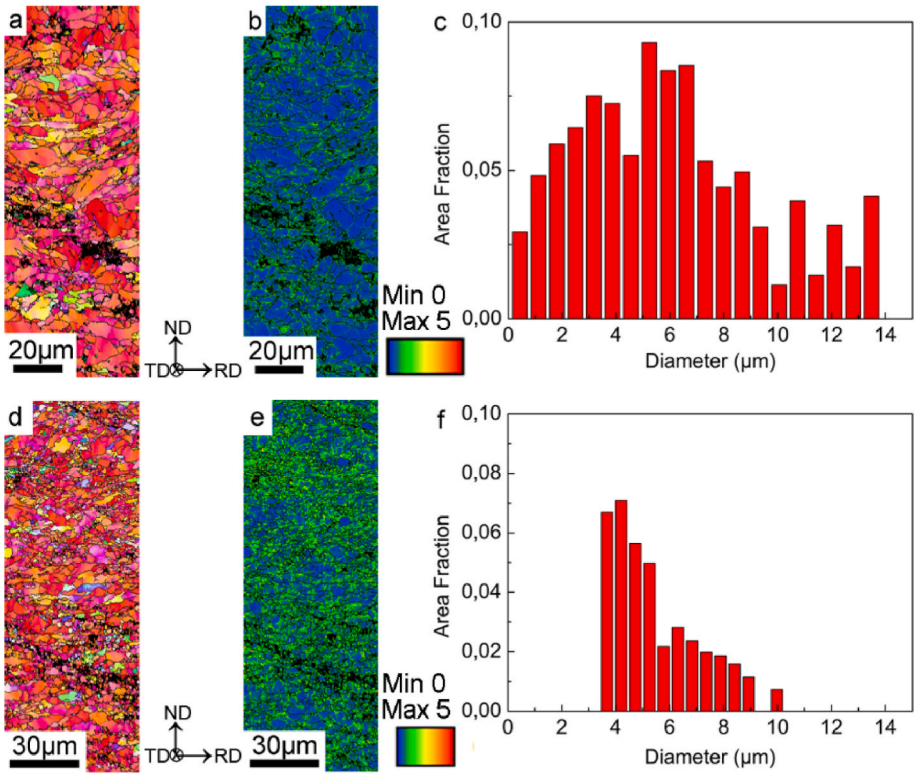

Fig. 6. IPF maps (a, d), KAM map (b, e), and the corresponding measured grain size distribution (c, f) of Mg–3Al–1Ca alloy (a–c) and Mg–3Al–1Ca–1Mn alloy (d–f) after the sixth rolling pass (with a total strain of 76% and at a temperature of 300 °C).

vicinity of the large Al_8Mn_5 phase, various nanoscale Ca-rich precipitates (also C15 Laves phase (Al_2Ca)) formed during rolling via dynamic precipitation were also observed. One typical HAADF-STEM image and the corresponding EDS maps of Mg, Al, Ca and Mn in Mg–3Al–1Ca–1Mn alloy after the sixth rolling pass is shown in Fig. S14.

3.6. TEM characterisation on the Mn-rich phases

Fig. 11 shows bright filed TEM image (Fig. 11a), corresponding SADP (Fig. 11b), HAADF-STEM image (Fig. 11c) and EDS maps (Fig. 11d–g) of large beta-Mn (Al_3Mn_6) phase (centre, left side) to Al_8Mn_5 phase (edge, right side) in Mg–3Al–1Ca–1Mn alloy after the sixth rolling pass. The beta-Mn phase (Al_3Mn_6) has the FCC structure (a = 0.6315 nm) with the mole ratios of Al and Mn about 40:60 [26]. Due to their large size, the beta-Mn (Al_3Mn_6) phase and the Al_8Mn_5 phase are more likely to be the primary phases formed during the solidification process. Interestingly, more Al is enriched at the edge, which can be seen in EDS map (Fig. 11e), strongly indicating the solute diffusion of Al from the beta-Mn (Al_3Mn_6) phase occurs, which forms Al_8Mn_5 phase. A similar observation has been reported in Ref. [49] where Al_8Mn_5 nucleates on B2–Al (Mn,Fe) particles and an incomplete peritectic transformation results in a Fe-richer B2–Al(Mn,Fe) core enveloped by a low-Fe Al_8Mn_5 shell.

Fig. 12 shows HAADF STEM image (Fig. 12a) and corresponding EDS maps (Fig. 12b–f) of the long plated-shaped Al_8Mn_5 phase in Mg–3Al–1Ca–1Mn alloy after the sixth rolling pass. Ca-rich particle was observed in the vicinity of the Al_8Mn_5 phase, which can be seen more clearly in Fig. 12f. The segregation of Ca atoms at the interface between the Mg matrix and the Al_8Mn_5 phase causes a decrease of the amount of Ca atoms dissolved into the Mg matrix. Such type of long plated-shaped Al_8Mn_5 phase forms via dynamic precipitation during the rolling process.

Fig. 13 shows HAADF STEM image (Fig. 13a) and corresponding EDS maps (Fig. 13b–e) of one nanoscale Mn-rich particle in Mg–3Al–1Ca–1Mn alloy after the sixth rolling pass. The Mn-rich particle was observed within the Mg matrix. Due to its small size, such type of Mn-rich particle can be regarded as clusters, which strengthens Mg–3Al–1Ca–1Mn alloy via clustering hardening as reported in Al alloy [51]. Such type of Mn-rich particle was also observed using APT.

3.7. APT characterisation of the Mn-rich phases

Fig. 14 shows 3D reconstruction of APT measurement for the Mg–3Al–1Ca–Mn alloy after the sixth rolling pass within the material volume containing one nano-sized Al_8Mn_5 particle. Fig. 14a–d shows distribution maps of Mg, Al, Ca, and Mn. Fig. 14e–h is enlarged to more clearly show distribution maps of Mg, Al, Ca, and Mn with the nano-sized Al_8Mn_5 particle. Fig. 14i shows 1D concentration profile measured by a cylinder of 2 nm in diameter marked across the Al_8Mn_5 phase in Fig. 14h. As shown in Fig. 14g, a trace Ca was observed around the Al_8Mn_5 phase. It should be noted here that the presence of Ca was observed only around the nanoscale Al_8Mn_5 phase, which may form via dynamic precipitation during rolling. For the large primary beta-Mn (Al_3Mn_6) phase and/or Al_8Mn_5 phase, no such type of Ca segregation was observed, as shown in Fig. S15. The measured composition ($(Al_{54}Ni_9)Mn_{37}$) is close to the Al_8Mn_5 phase. From Figs. S15b and c, Ni and Mn are enriched at the same region, indicating that Ni is present as an impurity although high purity materials were used in the present investigation. In addition, the Al_8Mn_5 phase is about 10 nm in thickness and 40 nm in length. When viewing from the thin side, the size is close to that of the Mn-rich particle observed in Fig. 13. Furthermore, it should be noted that, apart from the nano-sized Al_8Mn_5 particle, Al-rich clusters were also observed within Mg matrix, as shown in Fig. 14b, f.

3.8. APT characterisation of the Al-rich clusters

Fig. 15 shows 3D reconstruction of APT measurement for the Mg–3Al–1Ca–Mn alloy after the sixth rolling pass within the material volume containing Al-rich clusters. Fig. 15a shows the distribution map

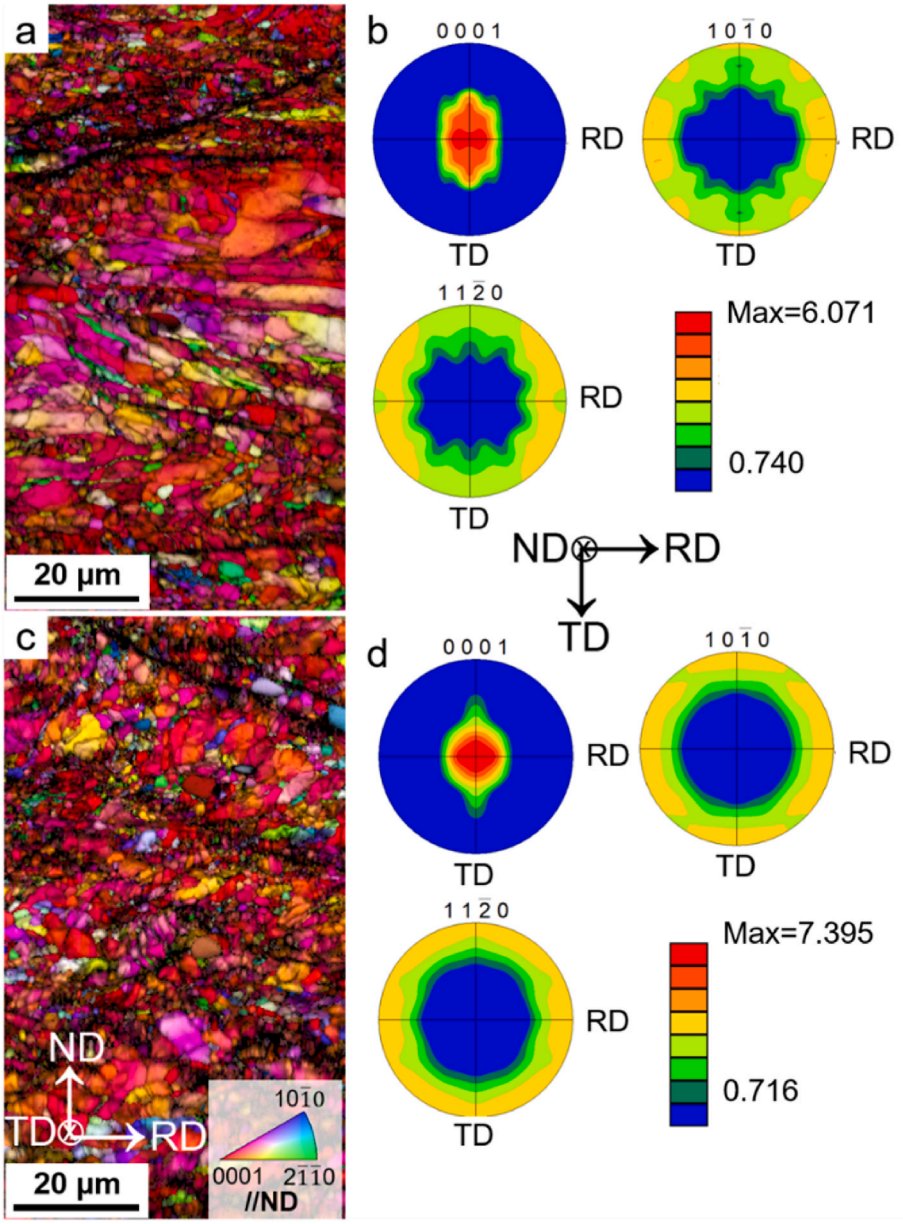

Fig. 7. IPF maps (a, c) and the corresponding {0001}, {10 $\bar{1}$ 0}, {11$\bar{2}$ 0} pole figures (b, d) of Mg–3Al–1Ca alloy (a, b) and Mg–3Al–1Ca–1Mn alloy (c, d) after the sixth rolling pass (with a total strain of 76% and at a temperature of 300 °C).

of Al within the detected Al-rich clusters. Fig. 15b shows randomized count as a function of d-pair (nm). Note that only Al solute was taken into consideration. Ca and Mn are not included for cluster analysis due to their absence within Mg matrix. The main cluster analysis parameters include: d-max: 0.74 nm, N-min: 12 ions, L: 0.74 nm, d-erosion: 0.74 nm. Most Al-rich clusters contain at least 12 solutes (Al) (see Fig. S16). These Al-rich clusters can be regarded as one type of G.P. zone, which form via dynamic precipitation during rolling and contribute to the strengthening effect via solute strengthening or clustering strengthening [51]. No Ca segregation into Al-rich cluster was observed, indicating that Ca does not partition into the Al-rich clusters after the sixth rolling pass at 300 °C. Further annealing treatment at higher temperatures (i.e. more than 300 °C) may motivate the partitioning of Ca into the Al-rich clusters and further improve the mechanical properties. Furthermore, no plate-shaped Ca-rich precipitate (i.e. on the basal plane of Mg matrix [28,33]) was observed within the detected region.

3.9. APT characterisation of the segregation of Al along grain boundaries

Fig. 16 shows 3D reconstruction of APT measurement for the Mg–3Al–1Ca–Mn alloy after rolling 6 passes within the material volume containing one grain boundary. Fig. 16a–d shows distribution maps of Mg and Al. Fig. 16c and d is enlarged from the region marked with a black box in Fig. 16b. Fig. 16e shows 1D concentration profile measured by a cylinder of 2 nm in diameter from the top to the bottom across the grain boundary in Fig. 16d. In Fig. 16e, the Mg element is higher than 98 at. %. and only Al element is shown. Clearly, a trace Al (up to 1.6 at. %) was observed along the grain boundary. The segregation of Al along grain boundaries increases the grain boundaries cohesion and thereby grain boundaries strengthening effect [6].

Similar to Fig. 15, Al-rich clusters was also determined using the same analysis procedure. Fig. 17 shows 3D reconstruction of APT measurement for the Mg–3Al–1Ca–Mn alloy after the sixth rolling pass within the material volume containing Al-rich clusters. Fig. 17a shows the distribution map of Al. Fig. 17b shows randomized count as a

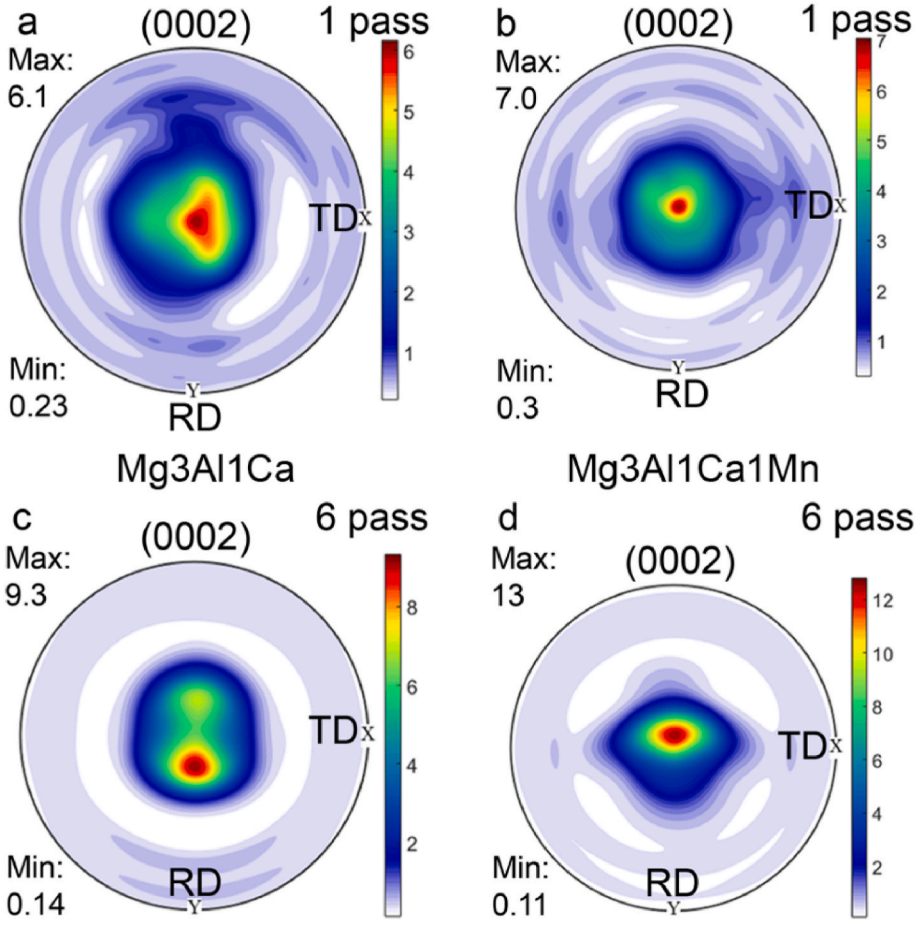

Fig. 8. {0002} pole figures of Mg–3Al–1Ca alloy (a, c) and Mg–3Al–1Ca–1Mn alloy (b, d) after the first rolling pass (a, b) (with a total strain of 24% (Mg–3Al–1Ca alloy (a)) and 20% (Mg–3Al–1Ca–1Mn alloy (b)), at a temperature of 350 °C) and sixth rolling pass (c, d) (with a total strain of 76% and at a temperature of 300 °C). X direction is along transverse direction, while Y direction is along rolling direction, which is different from Fig. 7.

function of d-pair (nm). Note that only Al solute was taken into consideration. The cluster analysis parameters include: d-max: 0.77 nm, N-min: 12 ions, L: 0.77 nm, d-erosion: 0.77 nm. Most Al-rich clusters contain at least 12 solutes (Al) (see Fig. S17).

4. Discussion

Compared with Mg–3Al–1Ca alloy after the first rolling pass, the yield strength of Mg–3Al–1Ca–1Mn alloy after the first rolling pass is much higher (89 MPa). While, compared with Mg–3Al–1Ca alloy after the sixth rolling pass, the yield strength of Mg–3Al–1Ca–1Mn alloy after the sixth rolling pass is only slightly higher (2 MPa). Clearly, there is a big difference of yield strength after the first rolling pass and this difference does not exist after the sixth rolling pass, strongly indicating that dynamic precipitation during rolling may play an important role for improving yield strength. According to the present detailed EBSD, XRD, TEM and APT characterization on the Mg–3Al–1Ca–1Mn alloy after the sixth rolling pass, possible reasons for this difference of yield strength can be discussed in terms of dispersion strengthening by the Ca-rich and Mn-rich phases, solid solution strengthening by Al-rich clusters, grain boundary strengthening by grain size and texture, respectively.

4.1. Grain boundary strengthening by grain size

After the first rolling pass, the grain size was measured to be about 10.5 ± 8.9 μm and 7.2 ± 7.4 μm for Mg–3Al–1Ca alloy and Mg–3Al–1Ca–1Mn alloy, respectively. According to the Hall-Petch relation [52], grain boundary strengthening by grain size can be evaluated as follow:

$$\sigma_y = \sigma_0 + kd^{-1/2} \quad (1)$$

where, σ_y is the yield stress, σ_0 is the friction stress for dislocation glide on the slip plane (10 MPa for Mg–Al based alloys [53]), d is the average grain size, and k is the Hall-Petch slope (235 MPa $\mu m^{1/2}$ [54,55]). The Hall-Petch slope k reflects the efficiency of grain boundary strengthening and has been reported to be highly changeable [56]. Thus, the grain boundary strengthening by grain size is calculated to be ~82 MPa and ~98 MPa for Mg–3Al–1Ca alloy and Mg–3Al–1Ca–1Mn alloy, respectively. The contribution to the difference of yield strength is only 16 MPa, which is much less than the measured difference of yield strength (89 MPa). After the sixth rolling pass, grain boundary strengthening by grain size is calculated to be ~106 MPa and ~139 MPa for Mg–3Al–1Ca alloy and Mg–3Al–1Ca–1Mn alloy, respectively. The contribution to the difference of yield strength is 33 MPa (two times higher than that after the first rolling pass), which is higher than the measured difference (2 MPa). This strongly indicates that other factors affecting strengthening effect have to be taken into consideration in order to interpret the difference of the yield strength after the first rolling pass.

4.2. Grain boundary strengthening by texture

Both micro-texture (EBSD) and macro-texture (XRD) analysis confirm that Mg–3Al–1Ca alloy has an RD-split texture, while Mg–3Al–1Ca–1Mn has a strong basal texture. The presence of RD-split

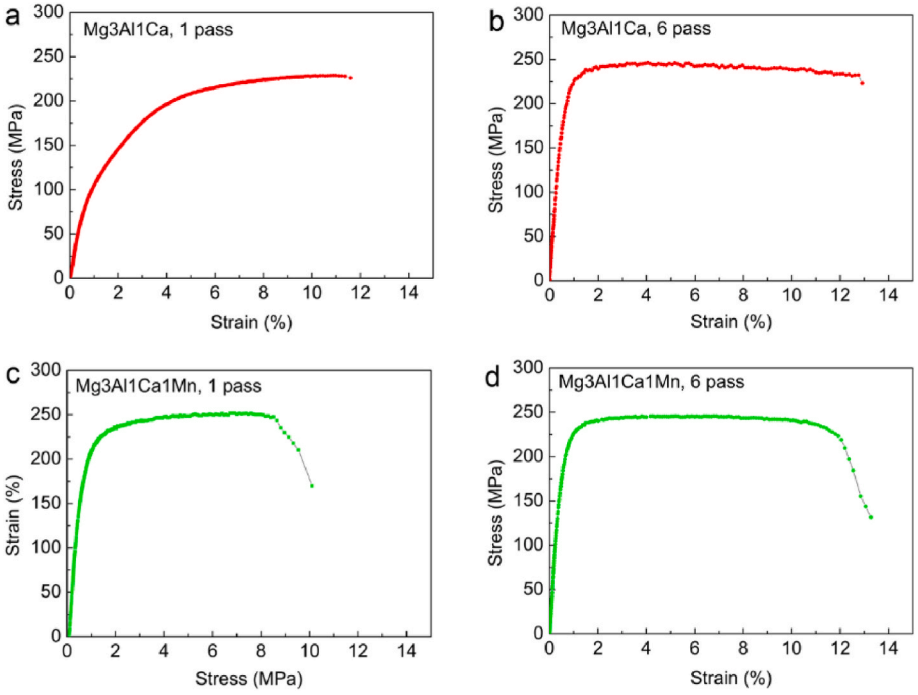

Fig. 9. Mechanical properties of Mg–3Al–1Ca alloy (a, b) and Mg–3Al–1Ca–1Mn alloy (c, d) after the first rolling pass (a, c) (with a total strain of 24% (Mg–3Al–1Ca alloy (a)) and 20% (Mg–3Al–1Ca–1Mn alloy (c)), at a temperature of 350 °C) and the sixth rolling pass (b, d) (with a total strain of 76% and at a temperature of 300 °C). All values were measured by DIC.

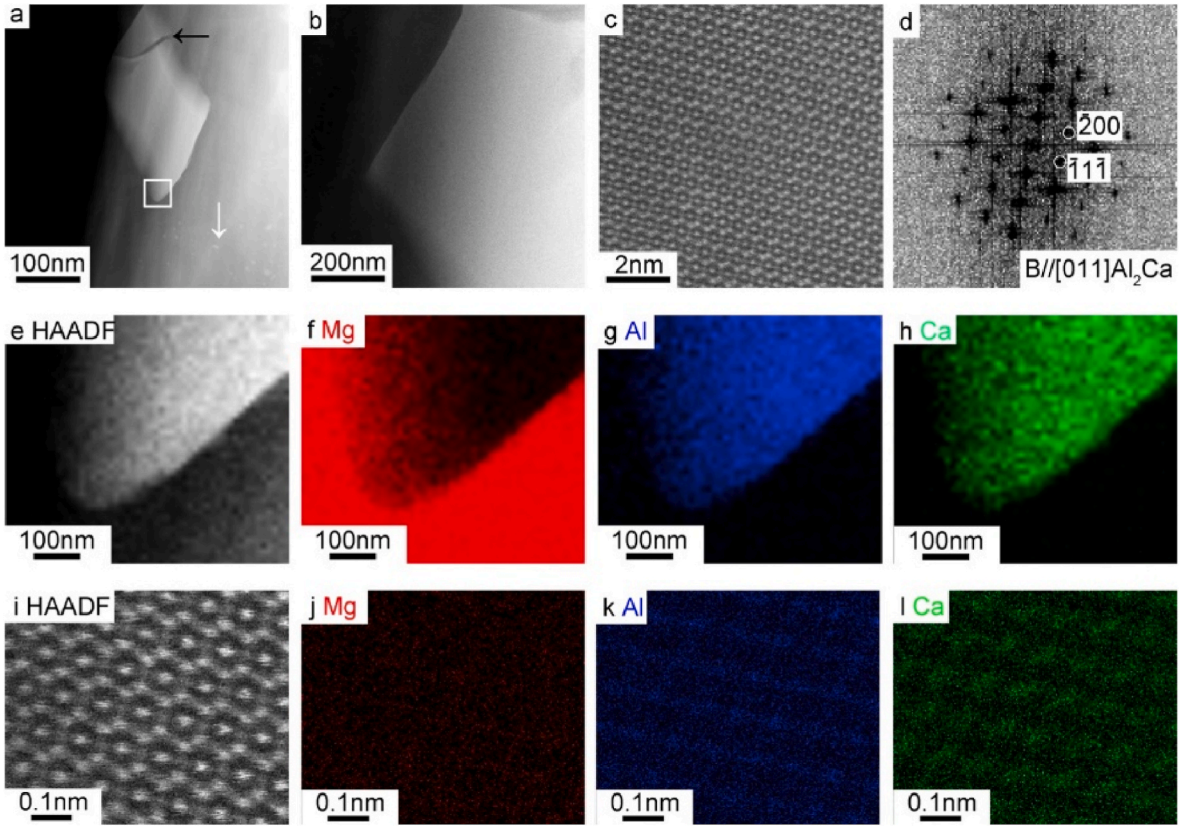

Fig. 10. (a, b, c) HAADF-STEM images, and (d) the corresponding FFT of (c), (e–h) low magnification HAADF-STEM image and EDS maps, and (i–l) high magnification HAADF-STEM image and EDS maps of C15 Laves phase (Al_2Ca) in Mg–3Al–1Ca–1Mn alloy after the sixth rolling pass (with a total strain of 76% and at a temperature of 300 °C). (b) is enlarged from the region marked with a white box in (a).

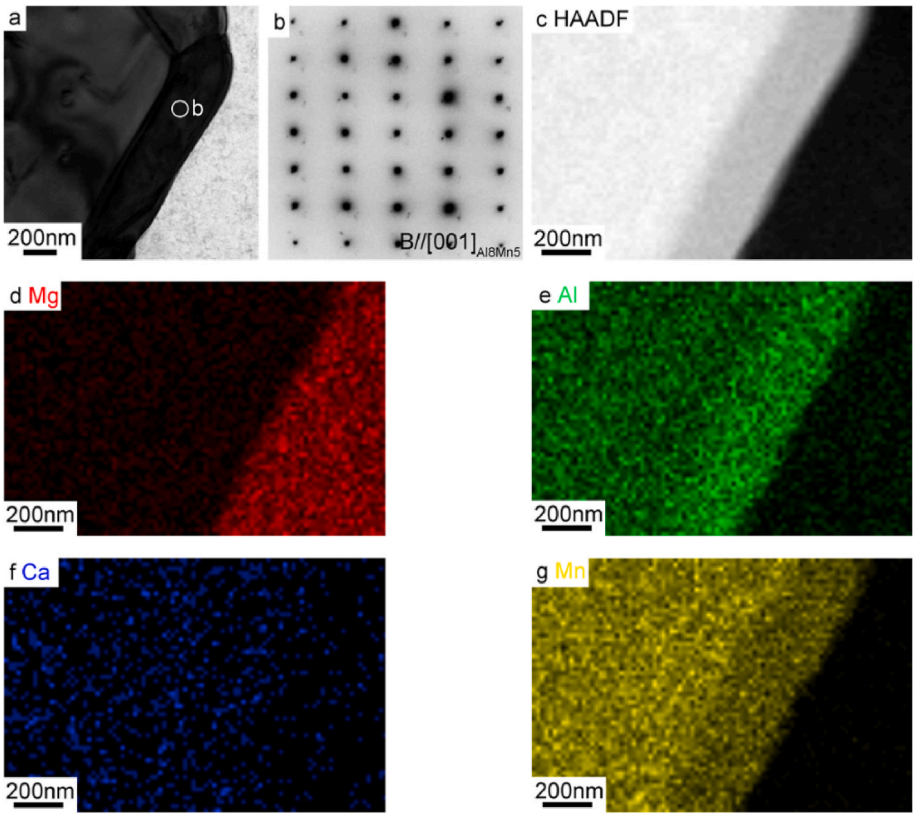

Fig. 11. (a) Bright filed TEM image, (b) corresponding SADP of the region as marked with a white circle in (a), (c) HAADF STEM image, (d–g) EDS maps showing the solute diffusion of Al from centre (the large primary beta-Mn (Al_3Mn_6) phase, cubic) to the edge (Al_8Mn_5 phase) in Mg–3Al–1Ca–1Mn alloy after the sixth rolling pass (with a total strain of 76% and at a temperature of 300 °C).

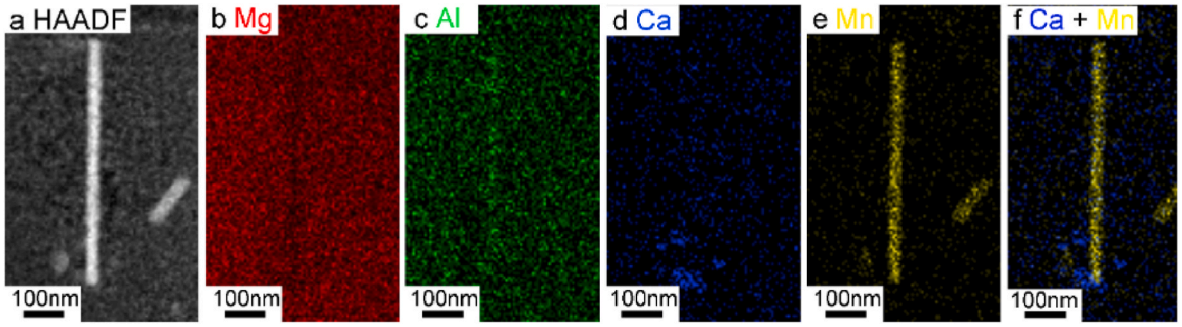

Fig. 12. (a) HAADF STEM image, (b–f) corresponding EDS maps of the long plate-shaped Al_8Mn_5 phase in Mg–3Al–1Ca–1Mn alloy after the sixth rolling pass (with a total strain of 76% and at a temperature of 300 °C). The blurring contrast in the HAADF-STEM image originates from Pt contamination caused by FIB.

texture has been reported in other Mg alloys containing Ca or RE elements and can be related to the presence of twins during recrystallization [32,37,39,57]. However, the presence of twins in Mg–3Al–1Ca alloy and Mg–3Al–1Ca–1Mn was rarely observed, especially after the sixth rolling pass, which can be due to the smaller grain size (10.5 ± 8.9 μm for Mg–3Al–1Ca alloy after the first rolling pass and 7.2 ± 7.4 μm for Mg–3Al–1Ca–1Mn alloy after the first rolling pass, 6.0 ± 3.4 μm for Mg–3Al–1Ca alloy after the sixth rolling pass, 3.3 ± 2.1 μm for Mg–3Al–1Ca–1Mn alloy after the sixth rolling pass) and dynamic recrystallization during rolling. In terms of grain size, it has been reported that a larger grain size is more favourable for the formation of twins [58]. Fine grains can prevent occurrence of twinning due to activation of non-basal slips. In terms of dynamic recrystallization, the temperature of deformation and the amount of strain are two key factors [59]. In the present investigation, the rolling temperature is 350 °C (for the first rolling pass) and 300 °C (for the sixth rolling pass). The dominant recrystallization mechanism is twin induced dynamic recrystallization (TDRX) and/or continuous dynamic recrystallization (CDRX). Although there is a slight difference of texture intensity in Mg–3Al–1Ca alloy and Mg–3Al–1Ca–1Mn alloys, there is no big difference of the texture evolution (see Figs. 5, 7 and 8 and Figs. S9–S11), which can be attributed to the fact that the solubility of Mn at the rolling temperature (350 °C or 300 °C) is very limited [60,61] and it does not affect the stacking-fault energy and thereby texture significantly [62,63]. The contribution to the difference of yield strength from the texture is insignificant. In order to ensure the solubility of Mn into Mg matrix and thereby tailor the texture evolution, a higher rolling temperature (higher than 500 °C) may be needed, which will be a further research work.

4.3. Solid solution strengthening by Al-rich clusters

Three alloying elements (Al, Ca, Mn) can be involved for solid

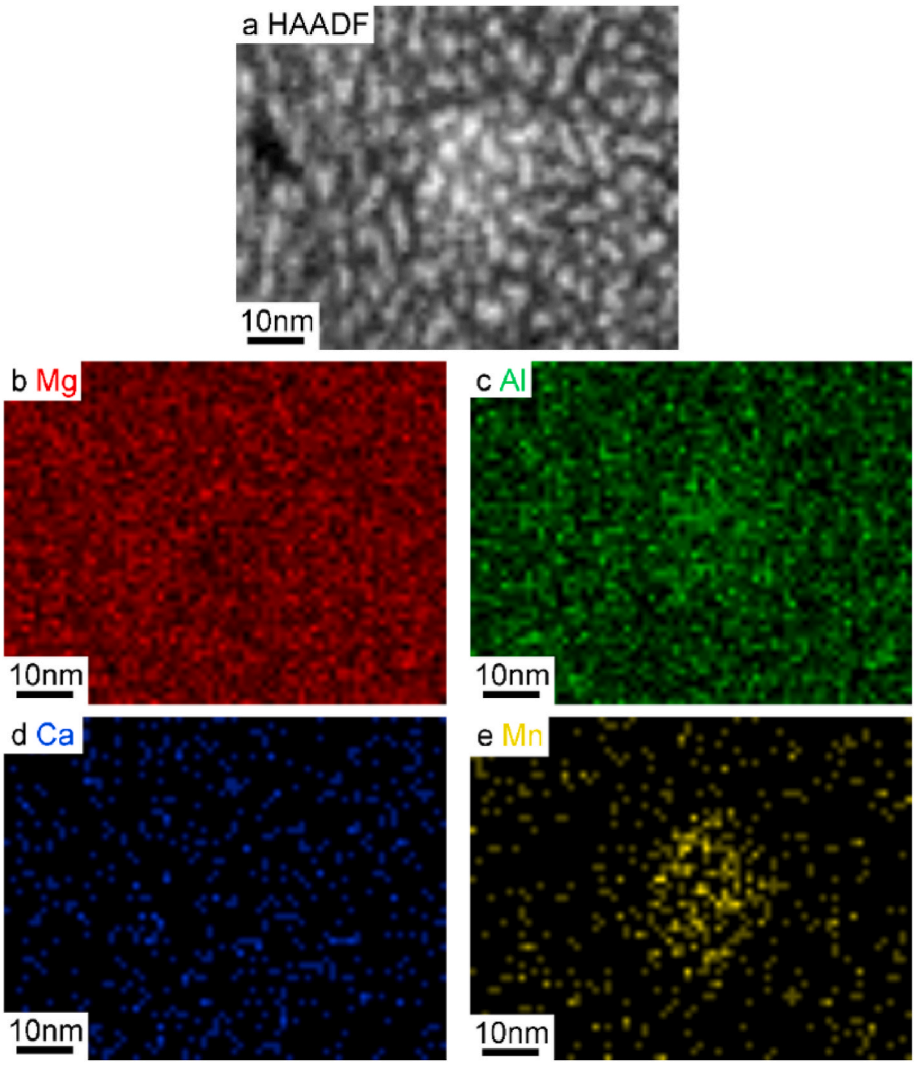

Fig. 13. (a) HAADF STEM image, (b–e) corresponding EDS maps of nanoscale Mn-rich phase (Al_8Mn_5) in Mg–3Al–1Ca–1Mn alloy after the sixth rolling pass (with a total strain of 76% and at a temperature of 300 °C).

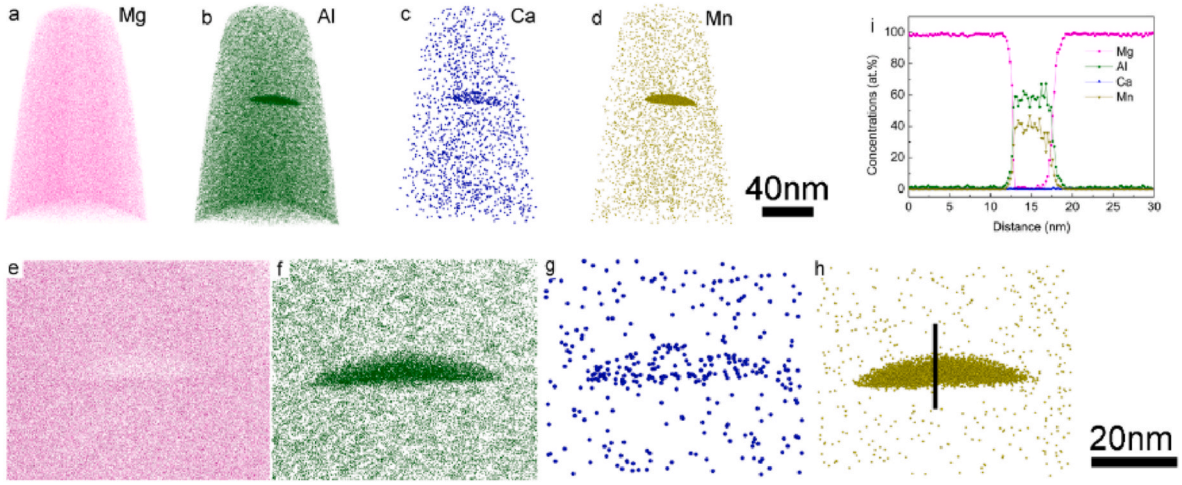

Fig. 14. 3D reconstruction of APT measurement for the Mg–3Al–1Ca–Mn alloy after the sixth rolling pass (with a total strain of 76% and at a temperature of 300 °C) within the material volume containing one nano-sized Al_8Mn_5 particle. (a-d, e-h) distribution maps of Mg, Al, Ca, and Mn. (i) 1D concentration profile measured by a cylinder of 2 nm in diameter marked across the Al_8Mn_5 phase in (h).

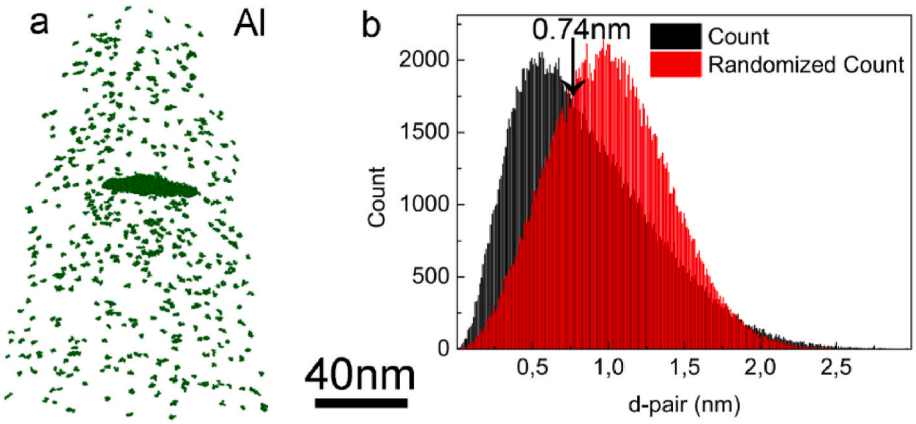

Fig. 15. 3D reconstruction of APT measurement for the Mg–3Al–1Ca–Mn alloy after the sixth rolling pass (with a total strain of 76% and at a temperature of 300 °C) within the material volume containing Al-rich clusters. (a) distribution maps of Al. (b) count and randomized count as a function of d-pair (nm) to distinguish the clusters from random distribution.

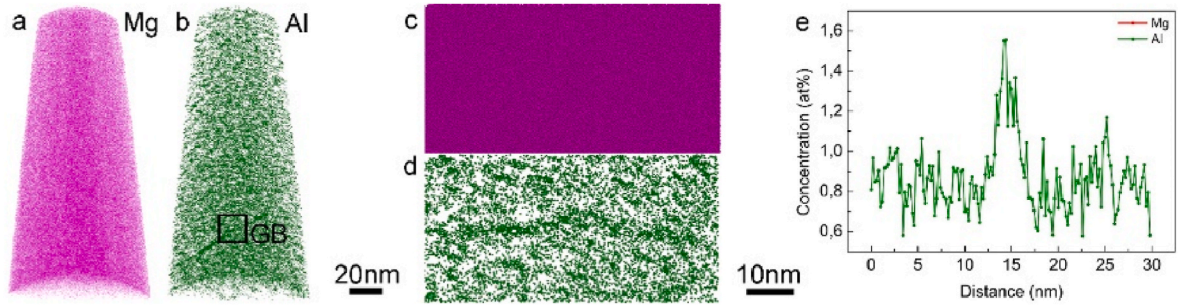

Fig. 16. 3D reconstruction of APT measurement for the Mg–3Al–1Ca–Mn alloy after the sixth rolling pass (with a total strain of 76% and at a temperature of 300 °C) within the material volume containing one grain boundary. (a–d) distribution maps of Mg and Al. (e) 1D concentration profile measured by a cylinder of 2 nm in diameter from the top to the bottom across the grain boundary in (d).

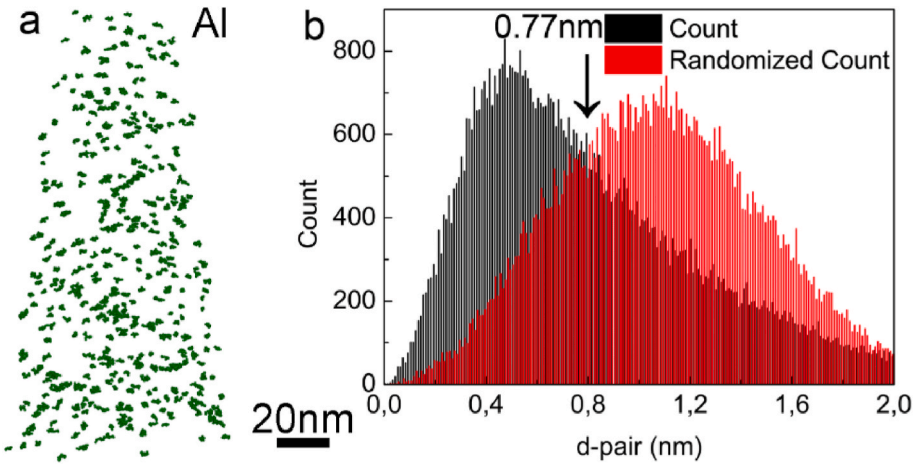

Fig. 17. 3D reconstruction of APT measurement for the Mg–3Al–1Ca–Mn alloy after the sixth rolling pass (with a total strain of 76% and at a temperature of 300 °C) within the material volume containing Al-rich clusters. (a) distribution maps of Al. (b) count and randomized count as a function of d-pair (nm) to distinguish the clusters from random distribution. Note that only Al solute was taken into consideration. The cluster analysis parameters include: d-max: 0.77 nm, N-min: 12 ions.

solution strengthening. In terms of Mn, the solubility of Mn in molten Mg has been reported in Ref. [60]. According to the derived experimental formulae for determining solubility of Mn in liquid Mg–Al alloys (Al contents: 5 wt. %, 9 wt. %, 11 wt. %) at different temperatures, in the present investigation, the solubility of Mn at 725 °C can be determined to be 1.15 wt. % (slightly higher than the addition level of Mn (1 wt. %) in the present investigation). But, at least two issues should be noted: (i) the Al content in the present investigation is only 3 wt. %, which is less than 5 wt. %, 9 wt. %, 11 wt. % in Ref. [60], and (ii) 1 wt. % Ca was also added in the present investigation, which also affects the solubility of Mn in molten Mg. According to Miedema et al. [64,65], the enthalpy of mixing between Mg and Mn is 35 kJ/g, while that between Ca and Mn is 59 kJ/g. Furthermore, the mixing enthalpy values of Al–Mn and Al–Ca are −70 and −20 kJ mol/1, respectively. This indicates that Mn and Ca

are more favourable to combine together with Al due to their large negative enthalpy of mixing. The calculated solubility of Mn (1.15 wt. %) in molten Mg in the present investigation may be therefore not eligible. Furthermore, with decreasing temperature, the solubility of Mn in Mg matrix decreases sharply, which can be reflected by the Mg–Mn binary phase diagram in Mg-rich region (0–3.7 at. % Mn) [61]. At 300 °C, the solid solubility of Mn in Mg is only 0.04 or 0.05 at. % [61]. Clearly, the addition of 1 wt. % Mn into Mg–3Al–1Ca alloy is much higher than the solid solubility of Mn within Mg matrix. Therefore, large primary beta-Mn (Al_3Mn_6) (Fig. 11) and Al_8Mn_5 phase (Fig. 1) form during solidification process. This is consistent with our present observation that Mn combines together with Al and form beta-Mn (Al_3Mn_6) and/or Al_8Mn_5 phase. No significant Mn solubility was detected within Mg matrix. The contribution for solid solution strengthening from the solid solubility of Mn is insignificant.

In terms of Ca, the same is also true with the solid solubility of Ca [66]. On the other hand, the atomic size of Mn, Al and Ca is 53 pm, 174 pm and 231 pm, respectively, while the atomic size of Mg is 173 pm. The larger atomic size of Ca than Mg results in an increase of lattice parameter, as shown in Fig. S13. However, it should be noted that their atomic radius between Ca and Mg differ by about 33.5%. According to the Hume-Rothery rule [67], which states that two metals that differ by more than 15% in their atomic radius will not form solid solutions, Ca is not likely to be dissolved into Mg matrix, which is consistent with APT observation (Figs. 14 and 16) that no significant Ca was observed within Mg matrix, although trace Ca was observed in the vicinity of Mn-rich particles (Al_8Mn_5). The contribution for solid solution strengthening from the solid solubility of Ca is also insignificant.

In terms of Al, the solubility of Al within Mg matrix can be measured using APT (from Figs. 14 and 16) to be up to 1.18 at. %. Furthermore, the atomic size of Al (174 pm) is very close to that of Mg (173 pm). According to the Hume-Rothery rule, Al is likely to be dissolved into Mg matrix, which is also consistent with APT observation (Figs. 15 and 17) that Al-rich clusters are present. Al primarily acts as a solute solution strengthening element and improves strengthening effect by the shear modulus strengthening and chemical strengthening. However, the formation of Al-rich clusters can also cause a significant strengthening effect, similar to clustering hardening in Al alloys [51]. The effect of solid solution strengthening can be described by the model of Gypen and Deruyttere [68]:

$$\Delta\sigma = \left(\sum_i k_i^{\frac{1}{n}} C_i\right)^n \tag{2}$$

where k_i, C_i and n are the strengthening constant, concentration of solute i in at. % and a coefficient with the value of 2/3 [69]. The contribution of Al to solid solution strengthening is determined as:

$$\sigma_{ss} = \left(k_{Al}^{\frac{1}{n}} C_{Al}\right)^n \tag{3}$$

where k_{Al} is taken as 196 MPa (at. %)$^{-2/3}$ [70]. The solubility of Al in Mg at room temperature (C_{Al}) is 1.18 at. %. Thus, the calculated value of solid solution strengthening is about 10 MPa.

In addition, it should be noted that Al also segregates into grain boundary to improve the boundary strength which withstands the incompatibility stress at the boundaries. Furthermore, the segregated Al element at grain boundaries suppresses its movement during recrystallization, and contributes to the formation of rather weak texture, which is crucial in designing formable and strong Mg–Al–Ca–Mn based alloys.

4.4. Dispersion strengthening by Mn-rich particles and Ca-rich Laves phase

In terms of dispersion strengthening by Mn-rich phase, the addition of 1 wt. % Mn into Mg–3Al–1Ca alloy results in the formation of three different Mn-rich phases: (i) large primary beta Mn (Al_3Mn_6) phase and Al_8Mn_5 phase, (ii) the long plated-shaped Al_8Mn_5 phase, and (iii) nanoscale Al_8Mn_5 phase. In the first case, neither primary beta-Mn (Al_3Mn_6) phase nor primary Al_8Mn_5 phase are believed to be beneficial for the improvement of yield strength due to their large size and rare distribution. In the second and third cases, there is a Ca segregation at the interface between the Mg matrix and the Al_8Mn_5 phase. Especially, in the third case, so-called "Janus particles" (core (Al_8Mn_5)-shell (Ca-rich layer) structure) can be very beneficial for the improvement of yield strength. Indeed, the yield strength of Mg–3Al–1Ca–1Mn alloy is always higher than that of Mg–3Al–1Ca alloy, especially after the first rolling pass. With increasing the rolling pass, the large primary beta-Mn (Al_3Mn_6) phase and Al_8Mn_5 phase (in the first case) and the long plated-shaped Al_8Mn_5 phase (in the second case) become broken and fragmented. Finally, this type of "Janus particles" (in the third case) becomes dominant in the microstructure. Similar so-called "Janus particles" of the Mg_2Ca phase co-precipitated at the site of the Al_8Mn_5 dispersoids has been reported in Ref. [40]. In this sense, dispersion strengthening by the Mn-rich particles can cause a significant strengthening effect, similar to clustering hardening in Al alloys [51]. A quantitative investigation on the effect of this type of "Janus particles" on the yield strength can be described via Orowan strengthening [71],

$$\sigma_{orowan} = M\frac{Gb}{2\pi\sqrt{1-\nu}\left(\frac{0.953}{\sqrt{f}}-1\right)d_p} ln\frac{d_p}{b} \tag{4}$$

where M, G, ν, b, d_p and f are the average Taylor factor (~2.5 [71]), shear modulus (~1.66 × 10^4 MPa [72]), Poisson's ratio (~0.3 [71]), Burgers vector (3.2 × 10^{-10} [72]), diameter and volume fraction of precipitates. According to TEM results, the diameter of Mn-rich phase is evaluated to be about 100 nm and volume fraction of Mn-rich phase is evaluated to be about 1%. The calculated value is ~17 MPa. It should be noted here that the evolution of the diameter and volume fraction of Mn-rich phase is only based on the two-dimensional TEM images. A three-dimensional TEM tomography is still needed to obtain more precise evolution of the diameter and volume fraction of Mn-rich phase.

In terms of dispersion strengthening by the Ca-rich Laves phase, C36 Laves phase was observed in as cast condition, while C15 Laves phase was observed after homogenization. Clearly, there is a phase transformation from C36 Laves phase to C15 Laves phase during homogenization. However, either C36 Laves phase in as cast condition or C15 Laves phase after homogenization are large in size and distributed along grain boundaries. Their strengthening effect is insignificant. After the first rolling pass, the large C15 Laves phase becomes broken and fragmented (Fig. S2), however, the nano-scale C15 Laves phase formed via dynamic precipitation after the first rolling pass may be still not dominant in the microstructure. Therefore, the yield strength of Mg–3Al–1Ca alloy is much lower (89 MPa) than that of Mg–3Al–1Ca–1Mn alloy, which may already contain various Mn-rich phase because of the presence of 1 wt. % Mn. With increasing the rolling up to 6 passes, more C15 Laves phase becomes broken and fragmented on one hand, and on the other hand more nano-scale C15 Laves phase forms via dynamic precipitation, which becomes dominant in the microstructure and competes with the effect of Mn-rich phase in Mg–3Al–1Ca–1Mn alloy. Therefore, the yield strength Mg–3Al–1Ca–1Mn alloy after the sixth rolling pass is only slightly higher (2 MPa) than that of Mg–3Al–1Ca alloy after the sixth rolling pass. In this sense, dispersion strengthening by the Ca-rich Laves phase can also cause a significant strengthening effect. Similar to the Mn-rich phase, according to TEM and XRD results, the diameter of C15 Laves is evaluated to be about 200 nm and the volume fraction of C15 Laves is evaluated to be about 1.5%. The calculated value according to equation (4) is 12 MPa. Together with dispersion strengthening by Mn-rich phase, a total value of 29 MPa is evaluated, which is close to that in rolled Mg–Al–Sn–Ca alloy [73]. It should be noted that no plate-shaped Al–Ca precipitate was observed, which can be attributed to the fact that most of Al element is involved to form C15 Laves phase (Al_2Ca) or Al_8Mn_5 precipitates.

4.5. Other possible strengthening effect

Apart from the possible strengthening effect for yield strength as described above, dislocations are also present after rolling, which can also improve the yield strength. The geometrically necessary dislocation (GND) density can be calculated using equation [73]:

$$\rho_{GND} = \frac{2\theta_{KAM}}{xb} \quad (5)$$

where x is unit length (about 0.1 μm), which is equal to twice the step size (about 0.05 μm) used in EBSD [65,66], b is the Burgers vector (3.2×10^{-10} [20]) and θ_{KAM} is KAM (Figs. 4 and 6), which can be obtained from EBSD data. The yield strength (σ_ρ) can be evaluated as follow [20,67]:

$$\sigma_\rho = MaGb\sqrt{\rho} \quad (6)$$

where M, G, b and a are the average Taylor factor (~2.5 [71]), shear modulus (~1.66×10^4 MPa [72]), Burgers vector (3.2×10^{-10} [72]) and a numerical constant (0.2) [71]. For the samples after the first rolling pass, the evaluated dislocation strengthening is about 19 MPa and 20 MPa for Mg–3Al–1Ca alloy and Mg–3Al–1Ca–1Mn alloy, respectively, while, for the samples after the sixth rolling pass, the evaluated dislocation strengthening is about 27 MPa and 22 MPa for Mg–3Al–1Ca alloy and Mg–3Al–1Ca–1Mn alloy, respectively, which is close to the previous values (~26 MPa and ~25 MPa) in rolled Mg-4.5Al-1.5Sn and Mg-4.5Al-1.5Sn-0.5Ca alloys [73]. Within increasing the rolling pass from one to six, a larger increase (8 MPa, from 19 MPa to 27 MPa) of the evaluated dislocation strengthening was observed in Mg–3Al–1Ca alloy, while only a slight increase (2 MPa, from 20 MPa to 22 MPa) of the evaluated dislocation strengthening was observed in Mg–3Al–1Ca–1Mn alloy, indicating that a more uniform deformation may take place in Mg–3Al–1Ca–1Mn alloy, which is beneficial for the further alloy development of Mg–Al–Ca–Mn based alloys. It should be noted here that, in the present investigation, dislocation evolution has been just determined by using KAM analysis (EBSD) but no detailed TEM investigation on dislocation evolution (slip) and twinning was performed yet.

By summing up possible strengthening effects together, it can be found that, for the Mg–3Al–1Ca alloy after the first rolling pass, the predicted value is about 111 MPa, which is close to the experimentally measured value (109 MPa), while, for the Mg–3Al–1Ca–1Mn alloy after the first rolling pass, the predicted value is about 145 MPa, which is less than the experimentally measured value (199 MPa). For the Mg–3Al–1Ca alloy after the sixth rolling pass, the predicted value is about 155 MPa, which is less than the experimentally measured value (198 MPa), while, for the Mg–3Al–1Ca–1Mn alloy after the sixth rolling pass, the predicted value is about 200 MPa, which is less than the experimentally measured value (220 MPa).

5. Conclusion

We have investigated the dynamic precipitation and yield strength of rolled Mg–3Al–1Ca–1Mn alloy. The following conclusions can be drawn:

1. After the first and the sixth rolling pass, an effective grain refinement was observed with the addition of 1 wt. % Mn, which can be attributed to the enhanced dynamic recrystallization by PSN mechanism. Grain boundary strengthening by grain size increases the yield strength significantly but it is not responsible for the large difference of the yield strength after the first rolling pass.
2. Mg–3Al–1Ca alloy has an RD-split texture, while Mg–3Al–1Ca–1Mn has a strong basal texture. No significant twin after the sixth rolling pass was observed, which can be attributed to a smaller grain size and dynamic recrystallization during rolling.
3. Three different Mn-rich phases: (i) large primary beta-Mn (Al_3Mn_6) phase and Al_8Mn_5 phase, (ii) the long plated-shaped Al_8Mn_5 phase, and (iii) nanoscale Al_8Mn_5 phase, were observed. The long plated-shaped Al_8Mn_5 phase and nanoscale Al_8Mn_5 phase are proposed to be beneficial for the improvement of yield strength and mainly responsible for the large difference of the yield strength after the first rolling pass.
4. With increasing rolling up to 6 passes, large C15 Laves phase (Al_2Ca) becomes broken and fragmented, and nano-scale C15 Laves phase forms via dynamic precipitation. Both fragmented and nano-scale C15 Laves phase are proposed to be beneficial for the improvement of yield strength.
5. Al-rich clusters (G.P. zone) were observed, but no plate-shaped Al–Ca precipitate on the basal plane of Mg matrix was observed. There is a competition between the formation of Al-rich clusters (G.P. zone), plate-like Al–Ca precipitates, C15 Laves phase, and Mn–rich precipitate within Mg matrix. The formation of Al-rich clusters (G.P. zone) is proposed to be beneficial for the improvement of yield strength.

CRediT authorship contribution statement

Jiehua Li: Conceptualization, Data curation, Formal analysis, Investigation, Methodology, Project administration, Funding acquisition, Writing – original draft, Writing – review & editing. **Xuyang Zhou:** Investigation. **Jing Su:** Investigation. **Benjamin Breitbach:** Investigation. **Marta Lipińska Chwałek:** Investigation. **Huiyuan Wang:** Investigation. **Gerhard Dehm:** Resources, Funding acquisition, Writing – review & editing.

Declaration of competing interest

The authors declare that they have no known competing financial interests or personal relationships that could have appeared to influence the work reported in this paper.

Data availability

Data will be made available on request.

Acknowledgements

J.H. Li acknowledges the host from Prof Dierk Raabe, technical support from the staffs in Max-Planck Institut für Eisenforschung and the financial support from Humboldt Research Fellowships for Experienced Researcher, Austrian Science Fund (No. P 32378-N37), BMBWF (KR 06/2020). X. Zhou is supported by Alexander von Humboldt-Stiftung. Marta Lipińska-Chwałek and Gerhard Dehm acknowledge the financial support from the Deutsche Forschungsgemeinschaft (DFG) within the Collaborative Research Centre SFB 1394: Structural and Chemical Atomic Complexity - From Defect Phase Diagrams to Material Properties, project ID 409476157. STEM experiments were performed at the Ernst Ruska-Center (ER-C) for Microscopy and Spectroscopy with Electrons, Forschungszentrum Jülich (FZJ) in Germany. The ER-C beam-time access for J.H. Li was provided via the DFG Core Facility Project ER-C D-030 and funding from the European Union's Horizon 2020 research and innovation program under grant agreement No. 823717-ESTEEM3 (ID 543).

Appendix A. Supplementary data

Supplementary data to this article can be found online at https://doi.org/10.1016/j.msea.2022.143898.

References

[1] B.L. Mordike, T. Ebert, Magnesium: properties-applications-potential, Mater. Sci. Eng. 302 (2001) 37–45, https://doi.org/10.1016/S0921-5093(00)01351-4.
[2] J.F. Nie, Precipitation and hardening in Magnesium alloys, Metall. Mater. Trans. 43 (2012) 3891–3939, https://doi.org/10.1007/s11661-012-1217-2.

[3] G. Zhu, L. Wang, J. Wang, J. Wang, J. Park, X. Zeng, High deformable Mg-Al-Ca alloy with Al_2Ca precipitates, Acta Mater. 200 (2020) 236–245, https://doi.org/10.1016/j.actamat.2020.09.006.

[4] T. Trang, J. Zhang, J. Kim, A. Zargaran, J. Hwang, B. Suh, N. Kim, Designing a magnesium alloy with high strength and high formability, Nat. Commun. 9 (2018) 2522, https://doi.org/10.1038/s41467-018-04981-4.

[5] G. Zhu, L. Wang, H. Zhou, J. Wang, Y. Shen, P. Tu, H. Zhu, W. Liu, P. Jin, X. Zeng, Improving ductility of a Mg alloy via non-basal <a> slip induced by Ca addition, Int. J. Plast. 120 (2019) 164–179, https://doi.org/10.1016/j.ijplas.2019.04.020.

[6] S. Nandy, S. Tsai, L. Stephenson, D. Raabe, S. Zaefferer, The role of Ca, Al and Zn on room temperature ductility and grain boundary cohesion of magnesium, Journal of Magnesium and Alloys 9 (2021) 1521–1536, https://doi.org/10.1016/j.jma.2021.03.005.

[7] S. Sandlöbes, M. Friák, S. Korte-Kerzel, Z. Pei, J. Neugebauer, D. Raabe, A rare-earth free magnesium alloy with improved intrinsic ductility, Sci. Rep. 7 (2017), 10458, https://doi.org/10.1038/s41598-017-10384-0.

[8] H.C. Pan, G.W. Qin, Y.M. Huang, Y.P. Ren, X.C. Sha, X.D. Han, Z.Q. Liu, C.F. Li, X. L. Wu, H.W. Chen, C. He, L.J. Chai, Y.Z. Wang, J.F. Nie, Development of low-alloyed and rare-earth-free magnesium alloys, Acta Mater. 149 (2018) 350–363, https://doi.org/10.1016/j.actamat.2018.03.002.

[9] K. Maruyama, M. Suzuki, H. Sato, Creep strength of magnesium-based alloys, Metall. Mater. Trans. 33 (2002) 875–882, https://doi.org/10.1007/s11661-002-1020-6.

[10] B.L. Mordike, Creep-resistant magnesium alloys, Mater. Sci. Eng. 324 (2002) 103–112, https://doi.org/10.1016/S0921-5093(01)01290-4.

[11] S.M. Zhu, B.L. Mordike, J.F. Nie, Creep and rupture properties of a squeeze-cast Mg-Al-Ca alloy, Metall. Mater. Trans. 37 (2006) 1221–1229, https://doi.org/10.1007/s11661-006-1073-z.

[12] S.M. Zhu, B.L. Mordike, J.F. Nie, Creep properties of a Mg–Al–Ca alloy produced by different casting technologies, Mater. Sci. Eng. 483–484 (2008) 583–586, https://doi.org/10.1016/j.msea.2006.09.154.

[13] N.D. Saddock, A. Suzuki, J.W. Jones, T.M. Pollock, Grain-scale creep processes in Mg–Al–Ca base alloys: implications for alloy design, Scripta Mater. 63 (2010) 692–697, https://doi.org/10.1016/j.scriptamat.2010.03.055.

[14] T. Homma, S. Nakawaki, S. Kamado, Improvement in creep property of a cast Mg–6Al–3Ca alloy by Mn addition, Scripta Mater. 63 (2010) 1173–1176, https://doi.org/10.1016/j.scriptamat.2010.08.033.

[15] Y. Nakaura, A. Watanabe, K. Ohori, Effects of Ca,Sr additions on properties of Mg-Al based alloys, Mater. Trans. 47 (2006) 1031–1039, https://doi.org/10.2320/matertrans.47.1031.

[16] A. Suzuki, N.D. Saddock, J.W. Jones, T.M. Pollock, Phase equilibria in the Mg-Al-Ca ternary system at 773 and 673 K, Metall. Mater. Trans. 37 (2006) 975–983, https://doi.org/10.1007/s11661-006-0070-6.

[17] D. Kevorkov, M. Medraj, J. Li, E. Essadiqi, P. Chartrand, The 400 °C isothermal section of the Mg-Al-Ca system, Intermetallics 18 (2010) 1498–1506, https://doi.org/10.1016/j.intermet.2010.03.038.

[18] Y. Zhong, J. Liu, R.A. Witt, Y. Sohn, Z.K. Liu, Al_2(Mg,Ca) phases in Mg–Al–Ca ternary system: first-principles prediction and experimental identification, Scripta Mater. 55 (2006) 573–576, https://doi.org/10.1016/j.scriptamat.2006.03.068.

[19] H. Cao, C. Zhang, J. Zhu, G. Cao, S. Kou, R. Schmid-Fetzer, Y.A. Chang, Experiments coupled with modeling to establish the Mg-rich phase equilibria of Mg–Al–Ca, Acta Mater. 56 (2008) 5245–5254, https://doi.org/10.1016/j.actamat.2008.07.003.

[20] A. Suzuki, N.D. Saddock, J.W. Jones, T.M. Pollock, Structure and transition of eutectic Mg,Al_2Ca Laves phase in a die-cast Mg-Al-Ca base alloy, Scripta Mater. 51 (2004) 1005–1010, https://doi.org/10.1016/j.scriptamat.2004.07.011.

[21] J.R. TerBush, A. Suzuki, N.D. Saddock, J.W. Jones, T.M. Pollock, Dislocation substructures of three die-cast Mg–Al–Ca-based alloys, Scripta Mater. 58 (2008) 914–917, https://doi.org/10.1016/j.scriptamat.2008.01.015.

[22] S.M. Liang, R.S. Chen, J.J. Blandin, M. Suery, E.H. Han, Thermal analysis and solidification pathways of Mg–Al–Ca system alloys, Mater. Sci. Eng. 480 (2008) 365–372, https://doi.org/10.1016/j.msea.2007.07.025.

[23] Z.T. Jiang, B. Jiang, H. Yang, Q.S. Yang, J.H. Dai, F.S. Pan, Influence of the Al_2Ca phase on microstructure and mechanical properties of Mg–Al–Ca alloys, J. Alloys Compd. 647 (2015) 357–363, https://doi.org/10.1016/j.jallcom.2015.06.060.

[24] X.G. Min, Y.S. Sun, F. Xue, W.W. Du, D.Y. Wu, Analysis of valence electron structures (VES) of intermetallic compounds containing calcium in Mg-Al-based alloys, Mater. Chem. Phys. 78 (2003) 88–93, https://doi.org/10.1016/S0254-0584(02)00312-7.

[25] G.S. Han, D. Chen, G. Chen, J.H. Huang, Development of non-flammable high strength extruded Mg-Al-Ca-Mn alloys with high Ca/Al ratio, J. Mater. Sci. Technol. 34 (11) (2018) 2063–2068, https://doi.org/10.1016/j.jmst.2018.03.019.

[26] T. Nakata, C. Xu, Y. Matsumoto, K. Shimizu, T.T. Sasaki, K. Hono, S. Kamado, Optimization of Mn content for high strengths in high-speed extruded Mg-0.3Al-0.3Ca (wt%) dilute alloy, Mater. Sci. Eng. 673 (2016) 443–449, https://doi.org/10.1016/j.msea.2016.07.098.

[27] T. Nakata, C. Xu, R. Ajima, K. Shimizu, S. Hanaki, T.T. Sasaki, L. Ma, K. Hono, S. Kamado, Strong and ductile age-hardening Mg-Al-Ca-Mn alloy that can be extruded as fast as aluminum alloys, Acta Mater. 130 (2017) 261–270, https://doi.org/10.1016/j.actamat.2017.03.046.

[28] T. Homma, S. Nakawaki, K. Oh Ishi, K. Hono, S. Kamado, Unexpected influence of Mn addition on the creep properties of a cast Mg-2Al-2Ca (mass%) alloy, Acta Mater. 59 (2011) 7662–7672, https://doi.org/10.1016/j.actamat.2011.08.049.

[29] S.W. Xu, K. Oh-ishi, S. Kamado, F. Uchida, T. Homma, K. Hono, High-strength extruded Mg–Al–Ca–Mn alloy, Scripta Mater. 65 (2011) 269–272, https://doi.org/10.1016/j.scriptamat.2011.04.026.

[30] T. Nakata, C. Xu, R. Ajima, Y. Matsumoto, K. Shimizu, T.T. Sasaki, K. Hono, S. Kamado, Improving mechanical properties and yield asymmetry in high-speed extrudable Mg-1.1Al-0.24Ca (wt%) alloy by high Mn addition, Mater. Sci. Eng. 712 (2018) 12–19, https://doi.org/10.1016/j.msea.2017.11.085.

[31] H. Huang, H. Liu, C. Wang, J.P. Sun, J. Bai, F. Xue, J.H. Jiang, A. Ma, Potential of multi-pass ECAP on improving the mechanical properties of a high-calcium-content Mg-Al-Ca-Mn alloy, Journal of Magnesium and Alloys 7 (2019) 617–627, https://doi.org/10.1016/j.jma.2019.04.008.

[32] T. Homma, S. Hirawatari, H. Sunohara, S. Kamado, Room and elevated temperature mechanical properties in the as-extruded Mg–Al–Ca–Mn alloys, Mater. Sci. Eng. 539 (2012) 163–169, https://doi.org/10.1016/j.msea.2012.01.074.

[33] J. J Bhattacharyya, T. Nakata, S. Kamado, S.R. Agnew, Origins of high strength and ductility combination in a Guinier-Preston zone containing Mg-Al-Ca-Mn alloy, Scripta Mater. 163 (2019) 121–124, https://doi.org/10.1016/j.scriptamat.2019.01.013.

[34] C.C. Xiang, Z.D. Xiao, H.L. Ding, Z.J. Wang, Compressive properties and energy absorption characteristics of extruded Mg-Al-Ca-Mn alloy at various high strain rates, Materials 14 (2021) 87, https://doi.org/10.3390/ma14010087.

[35] Z.T. Li, X.D. Zhang, M.Y. Zheng, X.G. Qiao, K. Wu, C. Xu, S. Kamado, Effect of CaAl ratio on microstructure and mechanical properties of Mg-Al-Ca-Mn alloys, Mater. Sci. Eng. 682 (2017) 423–432, https://doi.org/10.1016/j.msea.2016.11.026.

[36] H. Liu, C. Sun, C. Wang, Y.H. Li, J. Bai, F. Xue, A.B. Ma, J.H. Jiang, Improving toughness of a Mg_2Ca-containing Mg-Al-Ca-Mn alloy via refinement and uniform dispersion of Mg_2Ca particles, J. Mater. Sci. Technol. 59 (2020) 61–71, https://doi.org/10.1016/j.jmst.2020.02.092.

[37] M.Z. Bian, T.T. Sasaki, B.C. Suh, T. Nakata, S. Kamado, K. Hono, A heat-treatable Mg-Al-Ca-Mn-Zn sheet alloy with good room temperature formability, Scripta Mater. 138 (2017) 151–155, https://doi.org/10.1016/j.scriptamat.2017.05.034.

[38] M.Z. Bian, T.T. Sasaki, T. Nakata, S. Kamado, K. Hono, Effects of rolling conditions on the microstructure and mechanical properties in a Mg–Al–Ca–Mn–Zn alloy sheet, Mater. Sci. Eng. 730 (2018) 147–154, https://doi.org/10.1016/j.msea.2018.05.065.

[39] T. Nakata, C. Xu, K. Suzawa, K. Yoshida, N. Kawabe, S. Kamdado, Enhancing mechanical properties of rolled Mg-Al-Ca-Mn alloy sheet by Zn addition, Mater. Sci. Eng. 737 (2018) 223–229, https://doi.org/10.1016/j.msea.2018.09.059.

[40] M. Cihova, R. Schäublin, L.B. Hauser, S.S.A. Gerstl, C. Simson, P.J. Uggowitzer, J. F. Löffler, Rational design of a lean magnesium-based alloy with high age-hardening response, Acta Mater. 158 (2018) 214–229, https://doi.org/10.1016/j.actamat.2018.07.054.

[41] A. Malik, U.M. Chaudry, K. Hamad, T.S. Jun, Microstructure features and superplasticity of extruded, rolled and SPD-processed magnesium alloys: a short review, Metals 11 (2021) 1766, https://doi.org/10.3390/met11111766.

[42] G. Nolze, R. Hielscher, Orientations - perfectly colored, J. Appl. Crystallogr. 49 (2016) 1786–1802, https://doi.org/10.1107/S1600576716012942.

[43] G.B. Thompson, M.K. Miller, H.L. Fraser, Some aspects of atom probe specimen preparation and analysis of thin film materials, Ultramicroscopy 100 (2004) 25–34, https://doi.org/10.1016/j.ultramic.2004.01.010.

[44] M. Schaffer, B. Schaffer, Q. Ramasse, Sample preparation for atomic-resolution STEM at low voltages by FIB, Ultramicroscopy 114 (2012) 62–71, https://doi.org/10.1016/j.ultramic.2012.01.005.

[45] Y.M. Chen, P.H. Chou, E.A. Marquis, Quantitative atom probe tomography characterization of microstructures in a proton irradiated 304 stainless steel, J. Nucl. Mater. 451 (2014) 130–136, https://doi.org/10.1016/j.jnucmat.2014.03.034.

[46] L.T. Stephenson, M.P. Moody, P.V. Liddicoat, S.P. Ringer, New techniques for the analysis of fine-scaled clustering phenomena within atom probe tomography (APT) data, Microsc. Microanal. 13 (2007) 448–463, https://doi.org/10.1017/S1431927607070900.

[47] E. Marquis, J. Hyde, Applications of atom-probe tomography to the characterisation of solute behaviours, Mater. Sci. Eng. R 69 (2010) 37–62, https://doi.org/10.1016/j.mser.2010.05.001.

[48] Y. Wang, M. Xia, Z. Fan, X. Zhou, G.E. Thompson, The effect of Al_8Mn_5 intermetallic particles on grain size of as-cast Mg–Al–Zn AZ91D alloy, Intermetallics 18 (2010) 1683–1689, https://doi.org/10.1016/j.intermet.2010.05.004.

[49] G. Zeng, J.W. Xian, C.M. Gourlay, Nucleation and growth crystallography of Al_8Mn_5 on B2-Al(Mn,Fe) in AZ91 magnesium alloys, Acta Mater. 153 (2018) 364–376, https://doi.org/10.1016/j.actamat.2018.04.032.

[50] D.H. StJohn, M. Qian, M.A. Easton, P. Cao, Z. Hildebrand, Grain refinement of magnesium alloys, Metall. Mater. Trans. A 36 (2005) 1669–1679, https://doi.org/10.1007/s11661-005-0030-6.

[51] P. Dumitraschkewitz, S.S.A. Gerstl, L.T. Stephenson, P.J. Uggowitzer, S. Pogatscher, Clustering in age-hardenable aluminum alloys, Adv. Eng. Mater. 20 (2018), 1800255, https://doi.org/10.1002/adem.201800255.

[52] N. Hansen, Hall–Petch relation and boundary strengthening, Scripta Mater. 51 (2004) 801–806, https://doi.org/10.1016/j.scriptamat.2004.06.002.

[53] W. Yuan, S.K. Panigrahi, J.Q. Su, R.S. Mishra, Influence of grain size and texture on Hall–Petch relationship for a magnesium alloy, Scripta Mater. 65 (11) (2011) 994–997, https://doi.org/10.1016/j.scriptamat.2011.08.028.

[54] H. Yu, C. Li, Y. Xin, A. Chapuis, X. Huang, Q. Liu, The mechanism for the high dependence of the Hall-Petch slope for twinning/slip on texture in Mg alloys, Acta Mater. 128 (2017) 313–326, https://doi.org/10.1016/j.actamat.2017.02.044.

[55] Y. Chai, B. Jiang, J. Song, B. Liu, G. Huang, D. Zhang, F. Pan, Effects of Zn and Ca addition on microstructure and mechanical properties of as-extruded Mg-1.0Sn alloy sheet, Mater. Sci. Eng., A 746 (2019) 82–93, https://doi.org/10.1016/j.msea.2019.01.028.

[56] Y. Wen, B. Guan, Y. Xin, C. Liu, P. Wu, G. Huang, Q. Liu. Solute atom mediate d Hall-Petch relations for magnesium binary alloys, Scripta Mater. 210 (2022), 114451, https://doi.org/10.1016/j.scriptamat.2021.114451.
[57] B.J. Kwak, S.H. Park, Y.H. Moon, J.H. Lee, T. Lee, Plastic anisotropy of multi-pass caliber-rolled Mg alloy with split texture distribution, Mater. Sci. Eng., A 788 (2020), 139496, https://doi.org/10.1016/j.msea.2020.139496.
[58] M.R. Barnett, A rationale for the strong dependence of mechanical twinning on grain size, Scripta Mater. 59 (2008) 696–698, https://doi.org/10.1016/j.scriptamat.2008.05.027.
[59] S.E. Ion, F.J. Humphreys, S.H. White, Dynamic recrystallisation and the development of microstructure during the high temperature deformation of magnesium, Acta Metall. 30 (1982) 1909–1919, https://doi.org/10.1016/0001-6160(82)90031-1.
[60] Y. Tamura, T. Haitani, N. Kono, Liquid solubility of manganese and its influence on grain size of Mg-Al alloys, Mater. Trans. 47 (2006) 1968–1974, https://doi.org/10.2320/matertrans.47.1968.
[61] A.A. Nayeb Hashemi, J.B. Clark, The Mg-Mn (Magnesium-Manganese) system, Bulletin of Alloy Phase Diagrams 6 (1985) 160–164.
[62] J. Zhang, Y. Dou, G. Liu, Z. Guo, First-principles study of stacking fault energies in Mg-based binary alloys, Comput. Mater. Sci. 79 (2013) 564–569, https://doi.org/10.1016/j.commatsci.2013.07.012.
[63] W.Y. Wang, S. Shang, Y. Wang, Z. Mei, K.A. Darling, L.J. Kecskes, S.N. Mathaudhu, X. Hui, Z. Liu, Effects of alloying elements on stacking fault energies and electronic structures of binary Mg alloys: a first principles study, Materials Research Letters 2 (2014) 29–36, https://doi.org/10.1080/21663831.2013.858085.
[64] A.R. Miedema, A simple model for alloys. I. Rules for the alloying behaviour of transition metals, Philips Tech. Rev. 33 (1973) 149–160.
[65] A.R. Miedema, A simple model for alloys. Il, the influence of ionicity on the stability and other physical properties of alloys, Philips Tech. Rev. 33 (1973) 196–202.
[66] M. Aljarrah, M. Medraj, Thermodynamic modelling of the Mg–Ca, Mg–Sr, Ca–Sr and Mg–Ca–Sr systems using the modified quasichemical model, Computer Coupling of Phase Diagrams and Thermochemistry 32 (2008) 240–251, https://doi.org/10.1016/j.calphad.2007.09.001.
[67] W. Hume-Rothery, H.M. Powell, On the theory of super-lattice structures in alloys, Z. für Kristallogr. - Cryst. Mater. 91 (1935) 23, https://doi.org/10.1524/zkri.1935.91.1.23.
[68] L.A. Gypen, A. Deruyttere, Multi-component solid solution hardening, J. Mater. Sci. 12 (1977) 1028–1033, https://doi.org/10.1007/BF00540987.
[69] L. Gao, R.S. Chen, E.H. Han, Effects of rare-earth elements Gd and Y on the solid solution strengthening of Mg alloys, J. Alloys Compd. 481 (1–2) (2009) 379–384, https://doi.org/10.1016/j.jallcom.2009.02.131.
[70] W.L. Cheng, Q.W. Tian, H. Yu, H. Zhang, B.S. You, Strengthening mechanisms of indirect-extruded Mg–Sn based alloys at room temperature, J. Magnes. Alloy 2 (2014) 299–304, https://doi.org/10.1016/j.jma.2014.11.003.
[71] Z.-M. Hua, B.-Y. Wang, C. Wang, C.-Y. Ma, P.-K. Ma, Z.-P. Guan, Y.-J. Li, J.-S. Li, H.-Y. Wang, Development of low-alloyed Mg–Zn–Ca–Sn–Mn alloy with high strength-ductility synergy by sub-rapid solidification and hot rolling, J. Alloys Compd. 855 (2021), https://doi.org/10.1016/j.jallcom.2020.157317.
[72] P.-Y. Wang, B.-Y. Wang, C. Wang, J.-G. Wang, C.-Y. Ma, J.-S. Li, M. Zha, H.-Y. Wang, Design of multicomponent Mg–Al–Zn–Sn–Bi alloys with refined microstructure and enhanced tensile properties, Mater. Sci. Eng., A 791 (2020) 426, https://doi.org/10.1016/j.msea.2020.139696.
[73] M. Zha, J.W. Liang, H. Xing, H. Xu, B. Jiang, C. Wang, H.L. Jia, H.Y. Wang, Spheroiding and refining of coarse CaMgSn phase in Mg–Al–Sn–Ca alloys for simultaneously improved strength and ductility via sub-rapid solidification and controlled rolling Materials, Science and Engineering: A 834 (2022), 142598, https://doi.org/10.1016/j.msea.2022.142598.